

1 Earth System Model Aerosol-Cloud Diagnostics Package 2 (ESMAC Diags) Version 2: Assessments of Aerosols, Clouds and 3 Aerosol-Cloud Interactions Through Field Campaign and Long- 4 Term Observations

5 Shuaiqi Tang¹, Adam C. Varble¹, Jerome D. Fast¹, Kai Zhang¹, Peng Wu¹, Xiquan Dong², Fan
6 Mei¹, Mikhail Pekour¹, Joseph C. Hardin³, and Po-Lun Ma¹

7 ¹Pacific Northwest National Laboratory, Richland, WA, USA

8 ²University of Arizona, Tucson, AZ, USA

9 ³Unaffiliated scientist

10 *Correspondence to:* Shuaiqi Tang (shuaiqi.tang@pnnl.gov)

11

12 **Abstract.**

13 Poor representations of aerosols, clouds and aerosol-cloud interactions (ACI) in Earth System Models
14 (ESMs) have long been the largest uncertainties in predicting global climate change. Huge efforts have
15 been made to improve the representation of these processes in ESMs, and key to these efforts is
16 evaluation of ESM simulations with observations. Most well-established ESM diagnostics packages focus
17 on the climatological features; however, they are lacking-of-the process-level understanding and
18 representations of aerosols, clouds, and ACI. In this study, we developed an ESM aerosol-cloud
19 diagnostics package (ESMAC Diags) to facilitate routine evaluation of aerosols, clouds and aerosol-cloud
20 interactions simulated by the Department of Energy's (DOE) Energy Exascale Earth System Model
21 (E3SM). This paper documents its version 2 functionality (ESMAC Diags v2), which has substantial
22 updates from its version 1 (Tang et al., 2022a). The simulated aerosol and cloud properties have been
23 extensively compared with in-situ and remote-sensing measurements from aircraft, ship, surface and
24 satellite platforms in ESMAC Diags v2. It currently includes six field campaigns and two permanent sites
25 covering four geographical regions: Eastern North Atlantic, Central U.S., Northeastern Pacific and
26 Southern Ocean, where frequent liquid or mixed-phase clouds are present and extensive measurements
27 are available from the DOE Atmospheric Radiation Measurement user facility and other agencies.
28 ESMAC Diags v2 generates various types of single-variable and multi-variable diagnostics, including
29 percentiles, histograms, joint histograms and heatmaps, to evaluate model representation of aerosols,
30 clouds, and ~~ACI~~aerosol-cloud interactions. Select examples highlighting ESMAC Diags capabilities are
31 shown using E3SM version 2 (E3SMv2). E3SMv2 in general can reasonably reproduces many observed
32 aerosol and cloud properties, with biases in some variables such as aerosol particle and cloud droplet sizes
33 and number concentrations. The coupling of aerosol and cloud number concentrations may be too strong
34 in E3SMv2, possibly indicating a bias in processes that control aerosol activation. Furthermore, the liquid
35 water path response to perturbed cloud droplet number concentration behaves differently in E3SMv2 and
36 observations, which warrants a further study to improve the cloud microphysics parameterizations in
37 E3SMv2.

38

39 **1. Introduction**

40 Poor representations of aerosols, clouds and aerosol-cloud interactions (ACI) in Earth System Models
41 (ESMs) have long been the largest uncertainties in predicting global climate change (IPCC, 2021).
42 Challenges come from several aspects: first, there are many aerosol properties (e.g., number, size, phase,
43 shape, composition) and cloud micro- and macro-physical properties (e.g., fraction, water content,
44 number and size of liquid and ice hydrometeors) that affect Earth’s climate. Coincident measurements of
45 these properties remain largely under-sampled due to substantial spatiotemporal variability and logistical
46 difficulties for making such measurements. Second, there are complex interactive processes between
47 aerosols, clouds, and ambient meteorological conditions, many of which are not fully understood, but are
48 critical to properly interpreting relationships between observable properties. Third, many ACI processes
49 are nonlinear, multi-scale processes that involve feedbacks depending on cloud types and meteorological
50 regimes, which also shift in space and time, presenting challenges for assessing causal effect and
51 representing such processes in ESMs.

52 Huge efforts have been made to improve the representation of aerosols, clouds and ACI in ESMs. Key to
53 these efforts is evaluation of ESM simulations with observations. Many modeling centers have developed
54 standardized diagnostics packages to document ESM performance. For aerosol and cloud properties, most
55 diagnostic packages rely heavily on satellite measurements as evaluation data (e.g., AMWG, 2021;
56 E3SM, 2021; Eyring et al., 2016; Gleckler et al., 2016; Maloney et al., 2019; Myhre et al., 2013; Schulz
57 et al., 2006). Satellite remote sensing measurements have global or near global coverage but limited
58 spatial and temporal resolution. They are also ~~unable-facing many challenges~~ to retrieve some variables,
59 especially for aerosol properties such as number concentration, size distribution, chemical composition
60 etc. Some recent studies (e.g., Choudhury and Tesche, 2022) have retrieved cloud condensation nuclei
61 (CCN) number concentration from satellite measurements, which provides a great addition to investigate
62 ACI in global scale. However, large uncertainties exist in satellite retrievals, even for more sophisticated
63 retrieved, while many cloud microphysical ~~retrievals-properties~~ such as droplet number concentration
64 ~~have large uncertainties~~ (e.g., Grosvenor et al., 2018). This limits their application to robustly quantify
65 aerosols, clouds and ACI processes. In-situ measurements from ground, aircraft or ship platforms from
66 field campaigns are also used in a few projects to evaluate ESMs (e.g., Reddington et al., 2017; Watson-
67 Parris et al., 2019; Tang et al., 2022a; Zhang et al., 2020). Some of these field campaigns were conducted
68 over remote or poorly sampled locations, which are highly valuable for model evaluation despite limited
69 spatial coverage and time periods. Moreover, the U.S. Department of Energy (DOE) Atmospheric
70 Radiation Measurement (ARM) user facility has conducted continuous field measurements at a few sites
71 for multiple years. These long-term high-resolution field measurements have also been demonstrated to
72 be valuable for evaluating ESMs (e.g., Zhang et al., 2020).

73 In response to the need for more ESM diagnostics for evaluating ACI processes, Tang et al. (2022a)
74 developed an ESM aerosol-cloud diagnostics package (ESMAC Diags) to facilitate the routine evaluation
75 of aerosols, clouds and ACI simulated by the Department of Energy’s (DOE) Energy Exascale Earth
76 System Model (E3SM, Golaz et al., 2019). It includes diagnostics that leverage in-situ measurements
77 from multiple platforms during six field campaigns since 2013, which are not included in previous
78 diagnostics tools (e.g., Reddington et al., 2017). Version 1 of ESMAC Diags (ESMAC Diags v1, Tang et
79 al., 2022a) mainly focuses on aerosol properties. We present here version 2 of ESMAC Diags (ESMAC
80 Diags v2) that is a direct extension of ESMAC Diags v1 with two major additions:

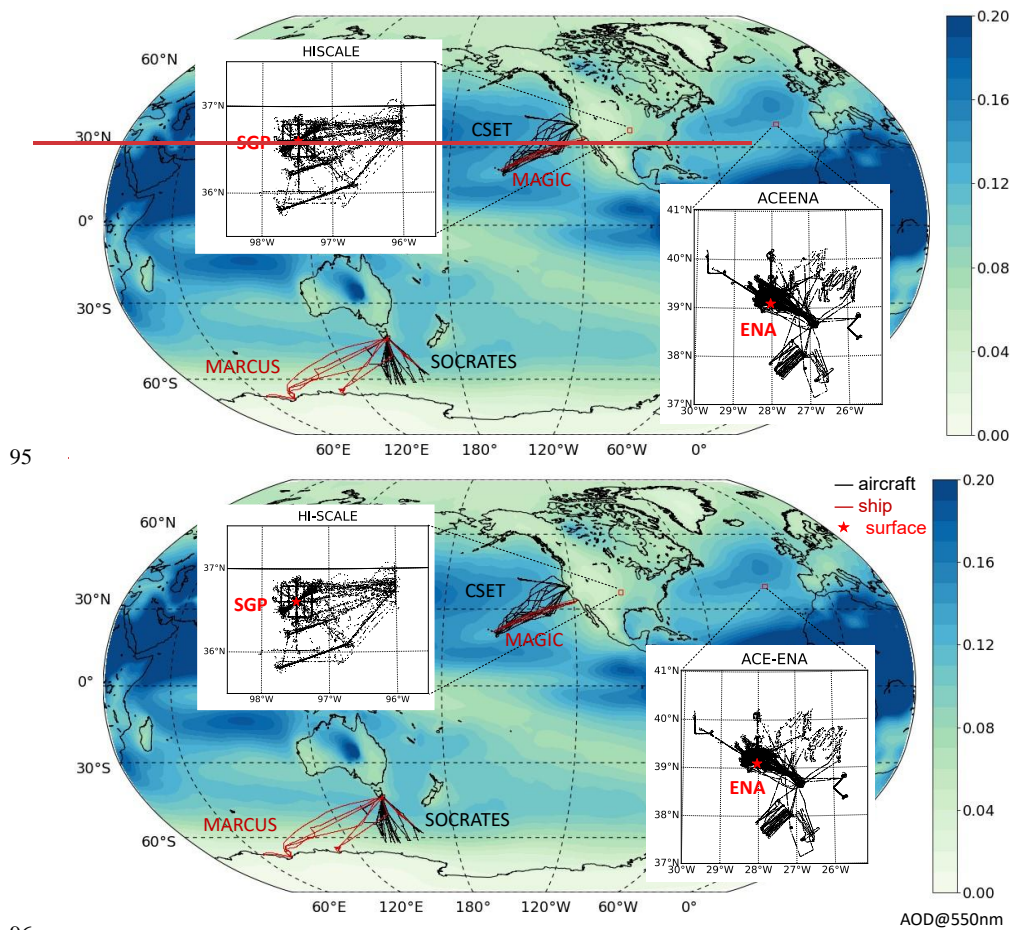
81 1. measurements from satellite and long-term diagnostics at the ARM Southern Great Plains
82 (SGP) and Eastern North Atlantic (ENA) sites.

83 2. diagnostics for cloud properties and aerosol-cloud interactions.

84 The new measurements, as well as major data quality controls are introduced in Section 2. Additional
85 discussions on retrieval uncertainties of cloud microphysical properties are performed in Section 3.
86 Details of the code structure of ESMAC Diags v2, which is substantially changed since version 1, are
87 described in Section 4. Section 5 provides selected examples of single-variable and multi-variable
88 diagnostics using ESMAC Diags v2 to highlight its capabilities. Lastly, Section 6 provides a summary.

89 **2. Aerosol and cloud measurements from ground, aircraft, ship and satellite platforms**

90 Following the initial development in version 1, ESMAC Diags v2 continues to focus on six field
91 campaigns conducted in four geographical regions: the Central U.S. (CUS, where the ARM Southern
92 Great Plains (SGP) site is located), Eastern North Atlantic (ENA), Northeastern Pacific (NEP), and
93 Southern Ocean (SO). Information on the six field campaigns is shown in Table 1 and their locations are
94 shown in Figure 1, each reproduced from Table 1 and Figure 3 in Tang et al. (2022a).



95
96
97 Figure 1. Aircraft (black) and ship (red) tracks for the six field campaigns. Red stars in
98 the enlarged map indicate two ARM fixed sites: SGP and ENA, that have long-term
99 measurements available for model diagnostics. Overlaid is aerosol optical depth at 550nm
100 averaged from 2014 to 2018 simulated in E3SMv1. (Reproduced from Figure 3 in Tang et
101 al., 2022a)

102 Table 1. Descriptions of the field campaigns used in this study. (Reproduced from Table 1
103 in Tang et al., 2022a)

Campaign*	Period	Platform	Typical Conditions	Reference
HI-SCALE	IOP1: 24 Apr – 21 May 2016	Ground, aircraft (IOP1: 17 flights, IOP2: 21 flights)	Continental cumulus with high aerosol loading	(Fast et al., 2019)

	IOP2: 28 Aug – 24 Sep 2016			
ACE-ENA	IOP1: 21 Jun – 20 Jul 2017 IOP2: 15 Jan – 18 Feb 2018	Ground, aircraft (IOP1: 20 flights, IOP2: 19 flights)	Marine stratocumulus with low aerosol loading	(Wang et al., 2021)
MAGIC	Oct 2012 – Sep 2013	Ship (18 legs)	Marine stratocumulus to cumulus transition with low aerosol loading	(Lewis and Teixeira, 2015; Zhou et al., 2015)
CSET	1 Jul – 15 Aug 2015	Aircraft (16 flights)	Same as above	(Albrecht et al., 2019)
MARCUS	Oct 2017 – Apr 2018	Ship (4 legs)	Marine liquid and mixed phase clouds with low aerosol loading	(McFarquhar et al., 2021)
SOCRATES	15 Jan – 24 Feb, 2018	Aircraft (14 flights)	Same as above	(McFarquhar et al., 2021)

104 * Full names of the listed field campaigns:

105 HI-SCALE: Holistic Interactions of Shallow Clouds, Aerosols and Land Ecosystems
106 ACE-ENA: Aerosol and Cloud Experiments in the Eastern North Atlantic
107 MAGIC: Marine ARM GCSS Pacific Cross-section Intercomparison (GPCI) Investigation of Clouds
108 CSET: Cloud System Evolution in the Trades
109 MARCUS: Measurements of Aerosols, Radiation and Clouds over the Southern Ocean
110 SOCRATES: Southern Ocean Cloud Radiation and Aerosol Transport Experimental Study
111

112 The collection and processing of observations are the most time-consuming part of developing ESMAC
113 Diags, which also impacts the reliability of conclusions drawn from the model diagnostics. In this section,
114 we introduce the data used in ESMAC Diags v2, existing quality issues in some datasets, and treatments
115 to address these quality issues. Some variables are difficult to directly measure or have limited in-situ
116 sampling and thus must be derived from remote sensing measurements using retrieval algorithms. In
117 Section 3, we further discuss the uncertainty and reliability of some cloud retrieval products via
118 comparisons with in-situ aircraft measurements.

119 2.1. Data availability

120 All measurements, instruments, and data products used in the six field campaigns and two long-term sites
121 in ESMAC Diags v2 are shown in Table 2. Further details of the measurements, data product names, and
122 DOIs are given in Tables S1 to S6 (for field campaigns) and Tables S7 and S8 (for SGP and ENA sites) in
123 the supplementary material. To allow maximum overlapping of key measurements while also ensuring a
124 long enough period for statistical evaluation, we select the periods of 1 Jan 2011 – 31 Dec 2020 for SGP
125 and 1 Jan 2016 – 31 Dec 2018 for ENA for long-term analyses. In addition to the aerosol measurements
126 discussed in Tang et al. (2022a), we incorporate more cloud and radiation measurements, as well as
127 geostationary satellite retrievals using Visible Infrared Solar-Infrared Split Window Technique (VISST)
128 (Minnis et al., 2008; Minnis et al., 2011) algorithm. The VISST products archived by ARM cover
129 approximately 10° by 10° regions in 0.5° by 0.5° resolution centered over ARM sites. Moreover, ARM
130 recently released products consisting of merged aerosol particle and cloud droplet size distributions from
131 aircraft measurements for HI-SCALE and ACE-ENA campaigns. These data are now used in ESMAC
132 Diags v2.

133 Table 2: List of instruments and measurements used in ESMAC Diags v2.

Platform	Measurements	Instruments / data products	Available campaigns
Ground	Surface temperature, relative humidity, wind, pressure, precipitation; upper-level temperature, relative humidity, wind	Surface meteorological station (MET), ARM best estimate (ARMBE) products	HI-SCALE, ACE-ENA, SGP, ENA
	Longwave and shortwave radiation, cloud fraction	ARM best estimate (ARMBE) products	HI-SCALE, ACE-ENA, SGP, ENA
	Aerosol number concentration	Condensation particle counter (CPC), Condensation particle counter – fine (CPCF), Condensation particle counter – ultrafine (CPCU), Ultra-high sensitivity aerosol spectrometer (UHSAS), Scanning mobility particle sizer (SMPS)	HI-SCALE, ACE-ENA, SGP, ENA
	Aerosol size distribution	Ultra-high sensitivity aerosol spectrometer (UHSAS), Scanning mobility particle sizer (SMPS), Nano scanning mobility particle sizer (nanoSMPS)	HI-SCALE, ACE-ENA, SGP, ENA
	Aerosol composition	Aerosol chemical speciation monitor (ACSM)	HI-SCALE, ACE-ENA, SGP, ENA
	CCN number concentration	Cloud condensation nuclei (CCN) counter	HI-SCALE, ACE-ENA, SGP, ENA
	Cloud optical depth	Multifilter rotating shadowband radiometer (MFRSR)	HI-SCALE, ACE-ENA, SGP, ENA
	Cloud droplet number concentration	Cloud droplet number concentration retrieval (Ndrop), cloud retrieval from Wu et al. (2020)	HI-SCALE, ACE-ENA, SGP, ENA
	Cloud droplet effective radius	Multifilter rotating shadowband radiometer (MFRSR), cloud retrieval from Wu et al. (2020)	HI-SCALE, ACE-ENA, SGP, ENA
	Cloud liquid water path	Microwave radiometer (MWR), ARM best estimate (ARMBE) products	HI-SCALE, ACE-ENA, SGP, ENA
	Cloud base height, cloud top height	Active remote sensing of clouds (ARSCL)	HI-SCALE, ACE-ENA, SGP, ENA
Satellite	TOA shortwave and longwave radiation	Geostationary satellite-based retrievals using Visible Infrared Solar-Infrared Split Window Technique (VISST) algorithm	HI-SCALE, ACE-ENA, MAGIC, MARCUS, SGP, ENA
	cloud fraction; height, pressure and temperature at cloud top	Geostationary satellite-based retrievals using Visible Infrared Solar-Infrared Split Window Technique (VISST) algorithm	HI-SCALE, ACE-ENA, MAGIC, MARCUS, SGP, ENA
	liquid water path; cloud optical depth; droplet effective radius	Geostationary satellite-based retrievals using Visible Infrared Solar-Infrared Split Window Technique (VISST) algorithm	HI-SCALE, ACE-ENA, MAGIC, MARCUS, SGP, ENA
	Cloud droplet number concentration	Retrieved from VISST data using the algorithm in Bennartz (2007)	HI-SCALE, ACE-ENA, MAGIC, MARCUS, SGP, ENA
Aircraft	Navigation information and meteorological parameters	Interagency working group for airborne data and telemetry systems (IWG)	HI-SCALE, ACE-ENA
	Aerosol number concentration	Condensation particle counter (CPC), Condensation particle counter – ultrafine (CPCU), Condensation nuclei counter (CNC), Ultra-high sensitivity aerosol spectrometer (UHSAS), Passive cavity aerosol spectrometer (PCASP)	HI-SCALE, ACE-ENA, CSET, SOCRATES
	Aerosol size distribution	Ultra-high sensitivity aerosol spectrometer (UHSAS), Fast integrated mobility spectrometer (FIMS), Passive cavity aerosol spectrometer (PCASP), Best estimate aerosol size distribution (BEASD)	HI-SCALE, ACE-ENA, CSET, SOCRATES

	Aerosol composition	High-resolution time-of-flight aerosol mass spectrometer (AMS)	HI-SCALE, ACE-ENA
	CCN number concentration	Cloud condensation nuclei (CCN) counter	HI-SCALE, ACE-ENA, SOCRATES
	Cloud liquid water content	Water content measuring system (WCM), PMS-King Liquid Water Content (LWC)	HI-SCALE, ACE-ENA, CSET, SOCRATES
	Cloud droplet number size distribution	1DC, 2DC, 2DS, CDP, Cloud probe merged size distribution (mergedSD)	HI-SCALE, ACE-ENA, CSET, SOCRATES
Ship	Navigation information and meteorological parameters	Meteorological station (MET)	MAGIC, MARCUS
	Aerosol number concentration	Condensation particle counter (CPC), Ultra-high sensitivity aerosol spectrometer (UHSAS)	MAGIC, MARCUS
	Aerosol size distribution	Ultra-high sensitivity aerosol spectrometer (UHSAS)	MAGIC, MARCUS
	CCN number concentration	Cloud condensation nuclei (CCN) counter	MAGIC, MARCUS
	Cloud liquid water path	Microwave radiometer (MWR)	MAGIC, MARCUS
	Cloud droplet number concentration, cloud effective radius	Cloud retrieval from Wu et al. (2020)	MAGIC

134

135 All the observational data are quality controlled with their time resolution re-scaled to that suitable for
136 evaluating E3SM, and the rescale resolution can be adjusted to fit for different model output frequencies.
137 Currently, ground, ship and satellite measurements are re-scaled to a 1-hour frequency which is
138 approximately to be consistent with 1-degree resolution current E3SM output frequency. Rescaling
139 consists of computing either the median, mean or interpolated value depending on the original data
140 frequency and variable properties. For most aerosol and cloud microphysics measurements, the median
141 value is computed to remove occasional spikes or zeros resulting from data contamination or
142 measurement error. For some bulk cloud properties (e.g., cloud fraction, liquid water path (LWP)), the
143 mean value is computed to be consistent with grid-mean E3SM output. Interpolation is only used when
144 the input frequency is equal to or coarser than the frequency of model output. For aircraft measurements,
145 1-minute resolution is used to retain high variability and allow matching samples of aerosol and cloud at
146 the same time. To compare with high-frequency aircraft data, E3SM output is interpolated to the
147 samedown-sealed to 1 minute resolution using the nearest grid cell and time slice. Although the current 1-
148 hour, 1-degree E3SM output could not capture the high variability of the aircraft measurements, we are
149 targeting the exascale E3SM version planned in the next few years. In kilometer scale resolution ESM
150 simulations, the high variability in aircraft measurements will be better captured. In the current
151 diagnostics we only focus on the statistics for the entire campaign. As seen later in Section 5.1, coarse-
152 resolution model outputs show similar percentile ranges with the high-resolution aircraft measurements,
153 indicating that for simple percentiles, large-scale variabilities dominate over subgrid variabilities over
154 month-long field campaign periods. Further analysis is needed to understand the importance of other
155 statistics (variance, covariance, etc.) of subgrid scale variabilities. The rescale resolution can be adjusted
156 in ESMAC Diags data preparation code for ESMs running at higher resolution (e.g., kilometer scale grid
157 spacing). All processed data are saved in a standardized NetCDF format (NETCDF, 2022) and available
158 for downloading (see data availability section) and direct use.

159 2.2 Data quality issues and treatments

160 Many observation datasets used in ESMAC Diags are ARM level-b (quality-controlled) or level-c (value-
161 added) products, which include quality control (QC) flags to indicate data quality issues. For most
162 datasets, a QC treatment is applied to remove all data with questionable flags. However, there are certain
163 datasets or circumstances in which a QC flag is overly strict (too many good data are removed) or not
164 strict enough (some bad data are not removed). Here we document some of these situations and how we
165 handle them in our data processing.

166 2.2.1 ARM Condensation Particle Counter (CPC) measurements

167 ARM CPC data have several QC values representing failure of different quality checks. One of them
168 checks if the concentration is greater than a maximum allowable value, which is set to $8,000 \text{ cm}^{-3}$ for
169 model 3010 (CPC, size detection limit 10 nm), $10,000 \text{ cm}^{-3}$ for model 3772 (CPCF, size detection limit 10
170 nm), and $50,000 \text{ cm}^{-3}$ for model 3776 (CPCU, size detection limit 3 nm). At SGP, new particle formation
171 (NPF) events occur frequently when CPC and CPCF measurements can exceed $30,000 \text{ cm}^{-3}$. This is much
172 higher than the maximum allowable value but physically reasonable. Simply removing these large values
173 results in an underestimation of aerosol number concentration and produces unrealistic diurnal cycle since
174 they usually occur during the daytime (Tang et al., 2022a). By consulting with the ARM instrument
175 mentor, we only remove data with critical QC flags, but keep data with this QC flag that is overly
176 restrictive.

177 2.2.2 NCAR research flight aerosol number concentration (CN) measurements

178 NCAR research flight (RF) data used in ESMAC Diags do not include QC flags but occasionally show
179 suspiciously large or negative aerosol counts. The following minimum and maximum thresholds are
180 applied to remove suspicious data:

- 181 • Total CN from a Condensation Nucleation Counter (CNC, reported as CONCN): minimum = 0,
182 maximum = $25,000 \text{ cm}^{-3}$.
- 183 • Total CN from an Ultra-High-Sensitivity Aerosol Spectrometer (UHSAS, reported as
184 UHSAS100): minimum = 0, maximum = $5,000 \text{ cm}^{-3}$.
- 185 • Aerosol number size distribution from an UHSAS (reported as CUHSAS_RWOOU or
186 CUHSAS_LWID): minimum = 0, maximum = 500 cm^{-3} per size bin.

187 2.2.3 Ship-measured aerosol properties

188 Aerosol instruments on ships are occasionally contaminated by ship emissions, which present as large
189 spikes in aerosol and CCN number concentrations. For ARM MARCUS measurements, Humphries
190 (2020) published reprocessed CN and CCN data to remove ship exhaust contamination using method
191 described in Humphries et al. (2019). This data is used in this diagnostics package. For MAGIC, we could
192 not find any ship exhaust contamination information. By visually examining the dataset, a simple
193 maximum threshold ($25,000 \text{ cm}^{-3}$ for CPC, $5,000 \text{ cm}^{-3}$ for UHSAS100, $2,000 \text{ cm}^{-3}$ for CCN at 0.1%
194 supersaturation and $4,000 \text{ cm}^{-3}$ for CCN at 0.5% supersaturation) is applied to remove likely
195 contamination from ship emissions.

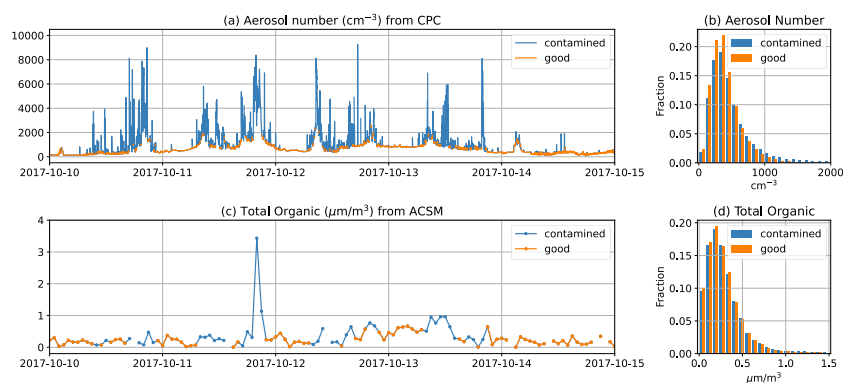
196 2.2.4 CCN measurements

197 There are different supersaturation (SS) setting strategies for CCN measurements. Some aircraft
 198 campaigns measured CCN with constant SS (ACE-ENA, HI-SCALE). Some other campaigns measured
 199 CCN with time-varying (scanning) SS (SOCRATES, surface CCN counters at SGP and ENA). However,
 200 the actual SS in a scanning strategy has fluctuations that are different than the target SS. For the latter,
 201 CCN for each SS (0.1%, 0.2%, 0.3% and 0.5%) are obtained by selecting CCN measured within $\pm 0.05\%$
 202 of the SS target.

203 For long-term measurements at SGP and ENA, near-hourly CCN spectra data are available, and a
 204 quadratic polynomial is fit to the spectra such that CCN number concentration can be estimated at any SS
 205 between the measured minimum and maximum SS values. We calculate and output CCN number
 206 concentration from these fits at three target supersaturations (0.1%, 0.2% and 0.5%). The fitted spectra
 207 data provides CCN number concentration at the exact target supersaturations, but the sample number is
 208 slightly smaller due to occasional failure of polynomial fitting.

209 2.2.5 Contaminated surface aerosol measurements at ENA

210 The ARM ENA site is located at a local airport. Aerosol measurements at ENA are sometimes
 211 contaminated by aircraft and vehicle emissions, rendering the measurements not representative of the
 212 background environment. Gallo et al. (2020) identified periods when CPC measurements were likely
 213 contaminated from localized emissions (Figure 2a). Their aerosol mask data has 1-min resolution. When
 214 we rescale the data to 1-hr resolution and apply the mask on other coarse time-resolution aerosol
 215 measurements (e.g., ACSM, Figure 2c), we mask hours in which more than half of the hour is flagged by
 216 the aerosol mask. The masking slightly increases the occurrence fraction of small values due to removing
 217 many large values, but it does not change the overall distribution (Figure 2b and 2d). A sensitivity
 218 analysis was performed, showing that 50% is a reasonable threshold to balance removal of contamination
 219 with keeping reasonable data (not shown).



220
 221 Figure 2: (a) CPC-measured CN from 10 to 15 October 2017 (1-minute resolution) with
 222 local contamination flagged by Gallo et al. (2020). (b) histogram of CPC-measured CN for
 223 all data from 2016-2018. (c) ACSM measured total organic matter from 10 to 15 October
 224 2017 (1-hour resolution). Hours with more than half of the hour flagged in 1-minute CPC

225 data are masked as contaminated. (d) histogram of ACSM-measured total organic matter
 226 for all data from 2016-2018.

227 3. Verification of cloud retrievals with in-situ measurements

228 Cloud microphysical properties such as droplet number concentration (N_d) and effective radius (R_{eff}) are
 229 important variables that connect clouds to other aspects in the climate system such as aerosols and
 230 radiation. Except in field campaigns where in-situ aircraft measurements are available, remote sensing
 231 retrieval algorithms are usually needed to derive these quantities. Several cloud retrieval products from
 232 ground and satellite measurements with different algorithms are used in ESMAC Diags v2. This section
 233 compares these cloud retrievals with in-situ aircraft measurements to assess retrieval limitation,
 234 uncertainty, and utility. N_d and R_{eff} from aircraft measurements taken during HI-SCALE and ACE-ENA
 235 field campaigns are calculated from merged cloud droplet number size distributions (mergedSD) from
 236 three different cloud probes with different size ranges. The mergedSD covers the size range from 1.5 μm
 237 to 9075 μm , covering the entire E3SM cloud droplet size distribution range and extending to rain droplet
 238 size range ($> 100 \mu\text{m}$). For field campaigns used in this study, the aircraft only flew through non-
 239 precipitating or drizzling clouds, in which the airborne measurements usually measure rain droplet
 240 number 3 to 5 orders of magnitude smaller than cloud droplet number. Therefore, the inclusion of rain
 241 droplet size range has ignorable impact on the aircraft-estimated N_d and R_{eff} .

242 Table 3 lists R_{eff} and N_d retrieval products used in ESMAC Diags v2. We retrieved N_{d_sat} with input
 243 data from VISST products using the algorithms described in Bennartz (2007), but assuming a ratio of the
 244 drop volume mean radius to R_{eff} (commonly referred to as k) of 0.74 and a cloud adiabaticity of 80%
 245 (Varble et al., 2023). Other datasets are all available as released products. All retrievals assume a
 246 horizontally homogeneous single-layer liquid phase cloud with constant N_d throughout the cloud layer.
 247 However, retrieval algorithms are usually run for all conditions whenever they return valid values. When
 248 assumptions are not satisfied, retrieved properties may contain large errors and likely alter statistics such
 249 as increasing the occurrence frequency of small N_d as will be shown next.

250 Table 3: Cloud droplet effective radius R_{eff} and number concentration N_d retrievals

Variable	Dataset	Platform	Campaign/site	Retrieved from	Reference
R_{eff}	MFRSRCLDOD	Ground	HI-SCALE, ACE-ENA, SGP, ENA	SW diffuse flux, LWP	(Min and Harrison, 1996; Turner et al., 2021)
	VISST	Satellite	HI-SCALE, ACE-ENA, MAGIC, MARCUS, SGP, ENA	Brightness temperature	(Minnis et al., 2011)
	Wu_etal	Ground	ACE-ENA, MAGIC, ENA	Radar reflectivity, LWP	(Wu et al., 2020)
N_d	Ndrop	Ground	HI-SCALE, ACE-ENA, SGP, ENA	LWP, COD, cloud height	(Riihimaki et al., 2021; Lim et al., 2016)
	N_{d_sat} (calculated from VISST)	Satellite	HI-SCALE, ACE-ENA, MAGIC, MARCUS, SGP, ENA	LWP, COD, CTT	(Bennartz, 2007)

	Wu_etal	Ground	ACE-ENA, MAGIC, ENA	Radar reflectivity, LWP	(Wu et al., 2020)
--	---------	--------	------------------------	----------------------------	-------------------

251 MFRSRCLDOD: Cloud Optical Properties from the MultiFilter Shadowband Radiometer (MFRSR)

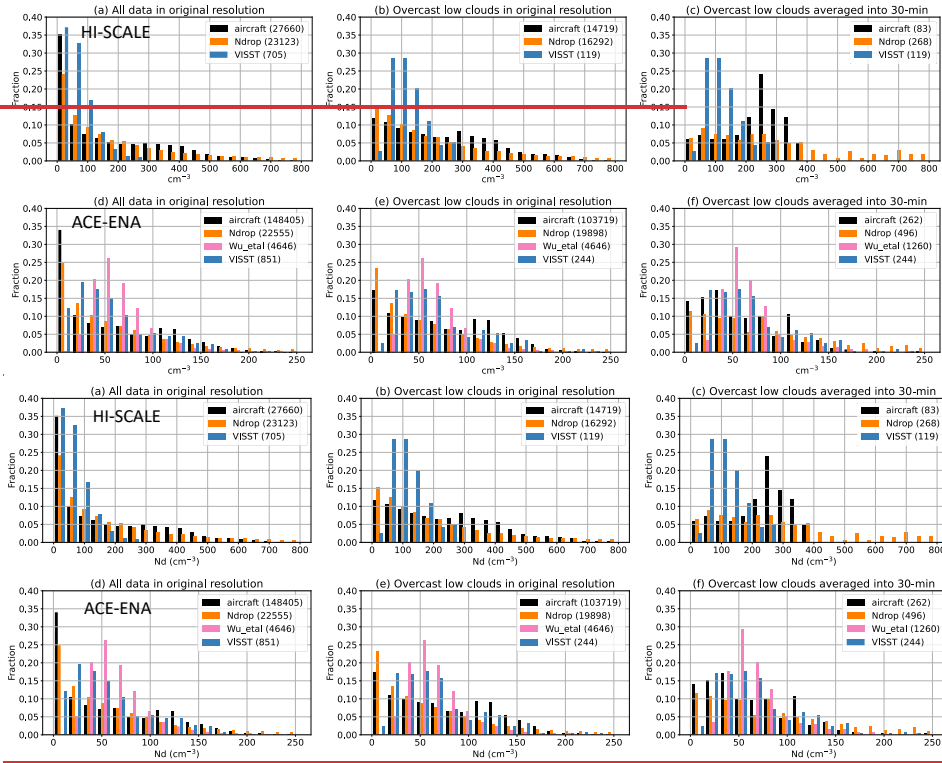
252 SW: shortwave

253 COD: cloud optical depth

254 CTT: cloud top temperature

255

256 Figures 3 shows the ~~probability density function (PDF)~~ occurrence fraction histograms of N_d retrievals
257 with aircraft measurements for HI-SCALE and ACE-ENA field campaigns, with the comparison of
258 original temporal resolution versus 30-minute mean, and the use of all available samples and samples that
259 are filtered as overcast (cloud fraction > 90%) low-level (cloud top height < 4 km) clouds. Figure 4 shows
260 similar plots but for R_{eff} . We also selected two cases with single-layer boundary layer stratus or
261 stratocumulus clouds and plotted their timeseries of original-resolution and 30-min averaged R_{eff} and N_d
262 in Figure S1. The high-frequency aircraft measurements and MFRSR/Ndrop retrievals exhibit much
263 larger variability than coarse-frequency retrievals of Wu_etal and VISST. They frequently sample cloud
264 edges or cloud top/base (for aircraft), where N_d is typically less than further into the cloud. This causes
265 large occurrence fractions in the lowest few bins in the N_d ~~PDFs~~ histograms (Figure 3a and 3d). The 30-
266 min VISST products also show large occurrence fraction in the lowest N_d bin for HI-SCALE (Figure 3a),
267 likely due to high frequency of partial cloudy condition over continental U.S. Filtering conditions to only
268 include overcast low-level clouds (Figure 3b, e) and averaging into a coarser resolution (Figure 3c, f) both
269 contribute to the reduction of occurrence fraction in small- N_d bins, and make the measurements from
270 different instruments more comparable.



271

272

273 Figure 3: Histogram of N_d from different measurements/retrievals in (top) HI-SCALE and
 274 (bottom) ACE-ENA field campaigns, with total sample numbers in the parentheses. (a) and
 275 (d) use data samples in their original resolution (1 s for aircraft measurements, 20 s for
 276 Ndrop data, 5 min for Wu_et al data, and 30 min for VISST data). (b) and (e) include only
 277 overcast low-cloud situations. For aircraft data, this means N_d is $> 1 \text{ cm}^{-3}$ for 5 s before
 278 and after the sampling time; for Ndrop and VISST data, it means cloud fraction $> 90\%$ and
 279 cloud top height $< 4\text{km}$. (c) and (f) include only overcast low-cloud situations, and
 280 average into 30-min resolution. For all the plots, VISST data with solar zenith angle $> 65^\circ$
 281 are removed to avoid artifact from sunlight.

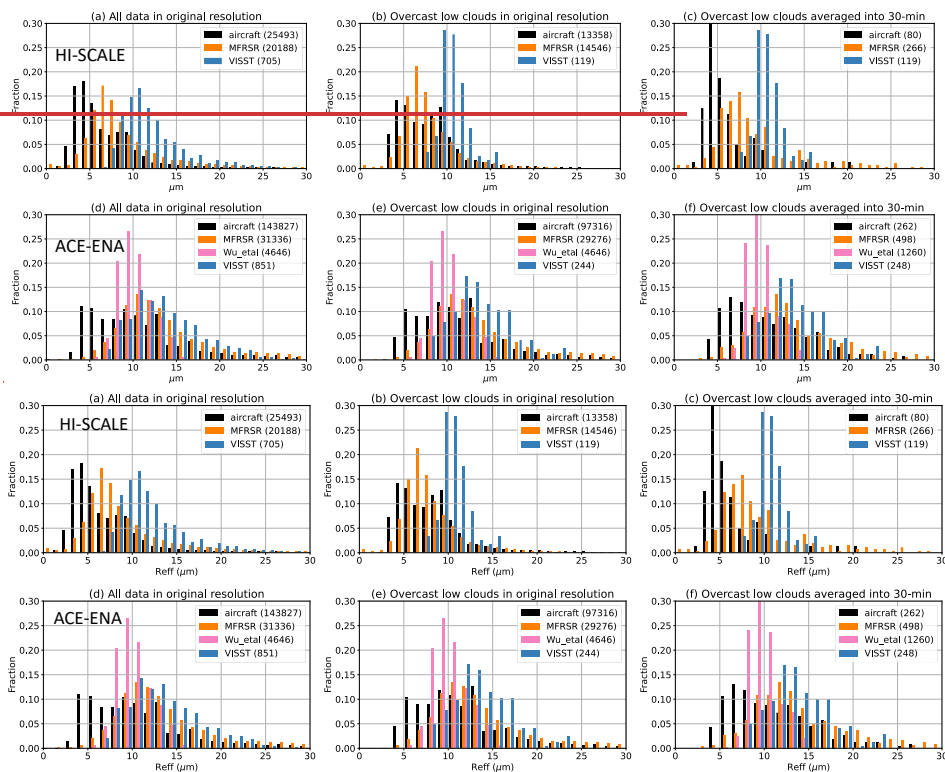


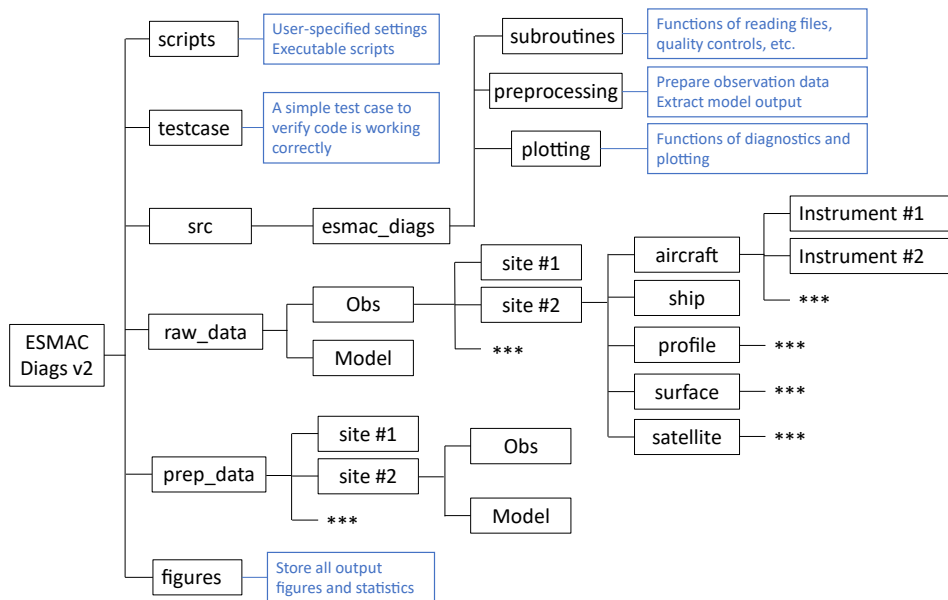
Figure 4: similar as in Figure 3 but for R_{eff} .

Overall, the remote sensing retrievals and aircraft measurements produce reasonable ranges of N_d and R_{eff} . Marine clouds (ACE-ENA) have smaller N_d (Figure 3) and larger R_{eff} (Figure 4) than continental clouds (HI-SCALE). Different retrievals are more consistent with each other for marine clouds than continental clouds. Different N_d datasets generally agree in mean value, but Even after rescaling to the same temporal resolution, aircraft and Ndrop data exhibit broader N_d distributions than satellite retrieval, likely due to their high sampling frequency that may capture more extreme conditions with very high or low N_d . Moreover, the assumption of a fixed adiabaticity (0.8) in satellite retrieval will also narrow N_d distribution. For R_{eff} , we do not expect different datasets to be perfectly agree with each other, as cloud droplet size grows with height in the cloud. All remote sensing retrievals have larger R_{eff} values than aircraft measurements, potentially because remote sensors weight more towards the upper cloud where droplet size and liquid water content (LWC) are larger. Wu_et al retrieves vertical profiles of R_{eff} , and a median value of the R_{eff} profile is used to represent the entire cloud. This makes Wu_et al retrieval weight less toward large droplets thus its R_{eff} is less than MFRSR and VISST. VISST data have the largest R_{eff} values, likely because satellite retrievals reflect conditions at the cloud top. Given the spread

299 in retrieved cloud properties, the limitations and uncertainties of cloud microphysics retrievals clearly
 300 need to be considered when they are used to evaluate model performances.

301 4. Structure of diagnostics package

302 Figure 5 shows the directory structure of ESMAC Diags v2. It is substantially changed from ESMAC
 303 Diags v1 (Tang et al., 2022a). First, we save all data separately as *raw_data*, which stores all input
 304 datasets collected from field campaigns, and *prep_data*, which stores preprocessed data with standardized
 305 time resolution and quality controls as described in Section 2. The structure is still designed to be flexible
 306 for future extension with additional measurements and/or functionality. Second, the diagnostics functions
 307 now give users more freedom to modify analyses, such as selecting different time periods, performing
 308 additional data filtering or treatments, and examining ACI relationships in specified variable
 309 combinations (for scatter plots, joint histograms or heatmaps). We provide a set of example scripts to
 310 assist users design their own diagnostics based on their needs. [We also provide the source code of data](#)
 311 [preparation for observations and model output, and a detailed instruction on how to run the code. Users](#)
 312 [can revise the code to process their own observational data or model output. All the information is](#)
 313 [available in the ESMAC Diags github repository.](#)



314
 315 Figure 5: Directory structure of ESMAC Diags v2. Blue boxes describe the functions of
 316 the directory. Asterisks represent boxes that follow the same format as those shown in
 317 parallel.

318 ESMAC Diags v1 included diagnostics of aerosol mean statistics (mean, bias, RMSE, correlation),
 319 timeseries, diurnal cycle, vertical profiles, mean particle number size distribution, percentiles by

320 height/latitude, and pie/bar charts (Tang et al., 2022a). ESMAC Diags v2 now includes the following new
321 diagnostics that include cloud variables:

- 322 - 5th, 25th, 50th, 75th and 95th percentiles,
- 323 - Seasonal cycle at SGP and ENA,
- 324 - Histograms for individual variables,
- 325 - Scatter plots,
- 326 - Joint histograms of two variables, and
- 327 - Heatmaps of three variables (mean of one variable binned by two other variables).

328 The inclusion of two-variable scatter plots, joint histograms, and three-variable heatmaps provides the
329 functionality to study ACI-related relationships. We present a few examples in the next section to
330 demonstrate these new diagnostics.

331

332 **5. Diagnostics Examples**

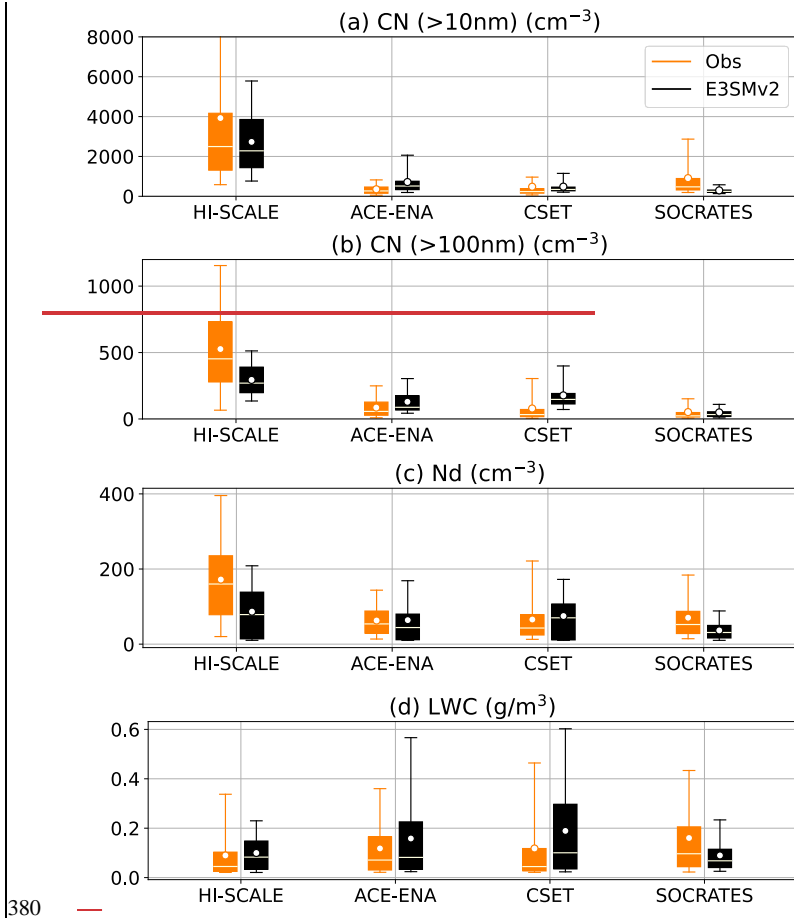
333 In this section, we show some examples of diagnostics applied to E3SM version 2 (E3SMv2) (Golaz et
334 al., 2022). Compared to the aerosol and cloud parameterizations in E3SMv1 (Rasch et al., 2019; Golaz et
335 al., 2019), E3SMv2 updated the treatments on dust particles, incorporated recalibration of parameters (Ma
336 et al., 2022), changed the call order and refactored the code of the Cloud Layers Unified By Binormals
337 (CLUBB) parameterization, and retuned some parameters (Golaz et al., 2022). We constrain the model
338 simulations by nudging the horizontal winds towards the 3-hourly Modern-Era Retrospective analysis for
339 Research and Applications, Version 2 (MERRA-2, Gelaro et al., 2017) with a nudging time scale of 6
340 hour. Previous studies have shown that with nudging, E3SM can well simulate the large-scale circulations
341 in reanalyses (Sun et al., 2019; Zhang et al., 2022). The model was run for individual field campaigns
342 (Table 1) and from 2010 to 2020 for long-term diagnostics at SGP and ENA sites, with hourly model
343 output saved over the field campaign regions for detail evaluation. As described in Section 2, all
344 diagnostics for ground and ship campaigns are in 1-hour resolution while diagnostics for aircraft
345 campaigns are in 1-minute resolution. For aerosol and cloud variables, model raw output variables (not
346 from instrument simulators) are used in this paper to reveal the intrinsic ACI relationships in E3SM.
347 However, as can be seen later in this section, instrument simulators can be better used in some diagnostics
348 to ensure more consistent comparison. Users may choose whether or not to use simulators in their
349 diagnostics depending on their purpose.

350 **5.1. Single-variable diagnostics**

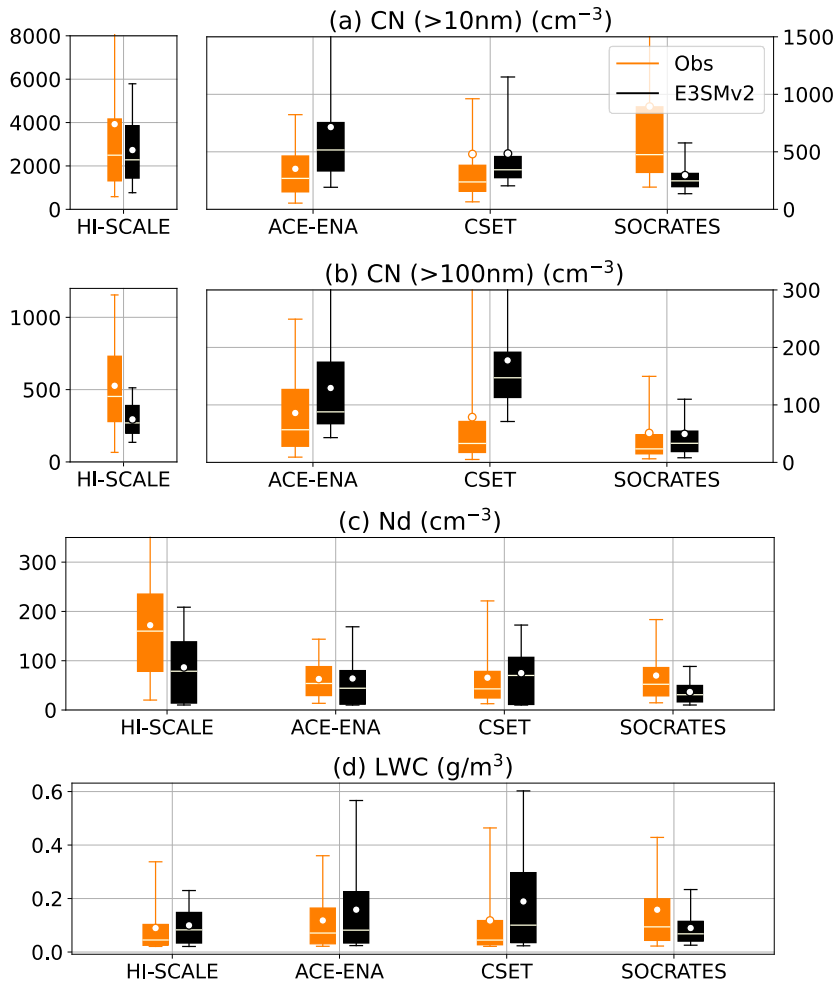
351 Figures 6 and 7 show mean and percentile values of aerosol and cloud properties measured from field
352 campaigns in the four geographical regions: CUS, ENA, NEP and SO. Figure 6 is for aircraft platforms
353 and Figure 7 is for ground or ship platforms with satellite data included when available. Note that the
354 aircraft and ground/ship campaigns may cover different time periods (Table 1), thus some differences
355 seen between aircraft and ship measurements may be caused by seasonal variation. As cloud
356 microphysical properties are usually retrieved with assumptions (Section 3), for ground/ship/satellite data,
357 we only focus on overcast low-level liquid cloud condition here (cloud fraction > 90%, cloud top height <
358 4 km and ice water path < 0.01 mm). E3SM does not output cloud top height, which is derived using a
359 weighting integration method as described in Varble et al. (2023).

360 From both aircraft and ground/ship data, HI-SCALE has much larger aerosol and cloud droplet number
361 concentrations with smaller droplet sizes compared to other campaigns, which is expected for a
362 continental environment compared to a marine environment. The cloud optical depth is also greater for
363 HI-SCALE than other campaigns, which is driven by smaller droplet sizes rather than LWP differences.
364 Satellite retrievals generally produce smaller N_d , LWP, and cloud optical depth with greater R_{eff} than
365 surface retrievals. As discussed in Section 3, retrieval uncertainties need to be kept in mind when these
366 retrieved microphysical properties are used to evaluate models.

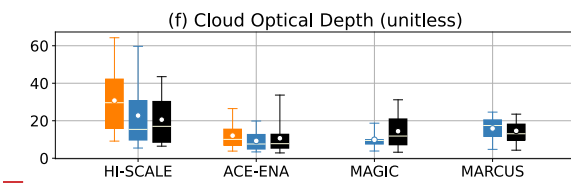
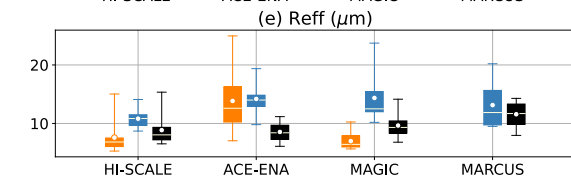
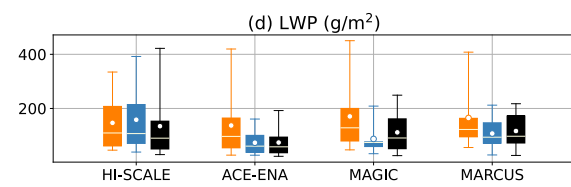
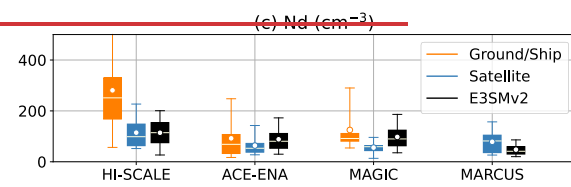
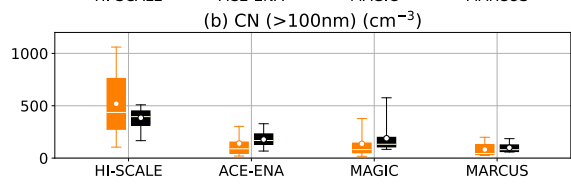
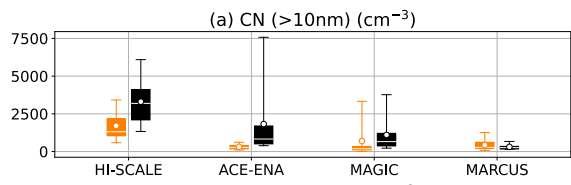
367 E3SMv2 overestimates CN (> 10 nm) over CUS, ENA and NEP. Larger particle concentration (CN > 100
368 nm) is generally underestimated over CUS and overestimated over ENA and NEP. Over SO, E3SMv2
369 produces fewer small aerosol particles (CN > 10 nm) and about the same number of large aerosol
370 particles (CN > 100 nm) compared to the observations. These results are confirmed by both aircraft and
371 ground/ship campaigns, except for the HI-SCALE aircraft campaign where small particles from local
372 emissions were occasionally observed but unable to be simulated. These results are consistent with our
373 previous diagnostics for E3SMv1 (Tang et al., 2022a). E3SMv2 also underestimates N_d over CUS and
374 SO, which corresponds with the underestimation of accumulation mode (> 100 nm) CN over CUS but
375 underestimation of Aitken mode (> 10 nm) CN over SO. It is possible that over very clean regions such as
376 SO, small particles are more important in cloud formation than over continental regions such as CUS.
377 Simulated LWP (LWC) is generally consistent with satellite (aircraft) measurements, but smaller than
378 ground/ship measurements, which may be partly caused by rain contamination of ground/ship retrievals.
379 R_{eff} evaluation is less certain given large discrepancies between satellite and ground retrievals.



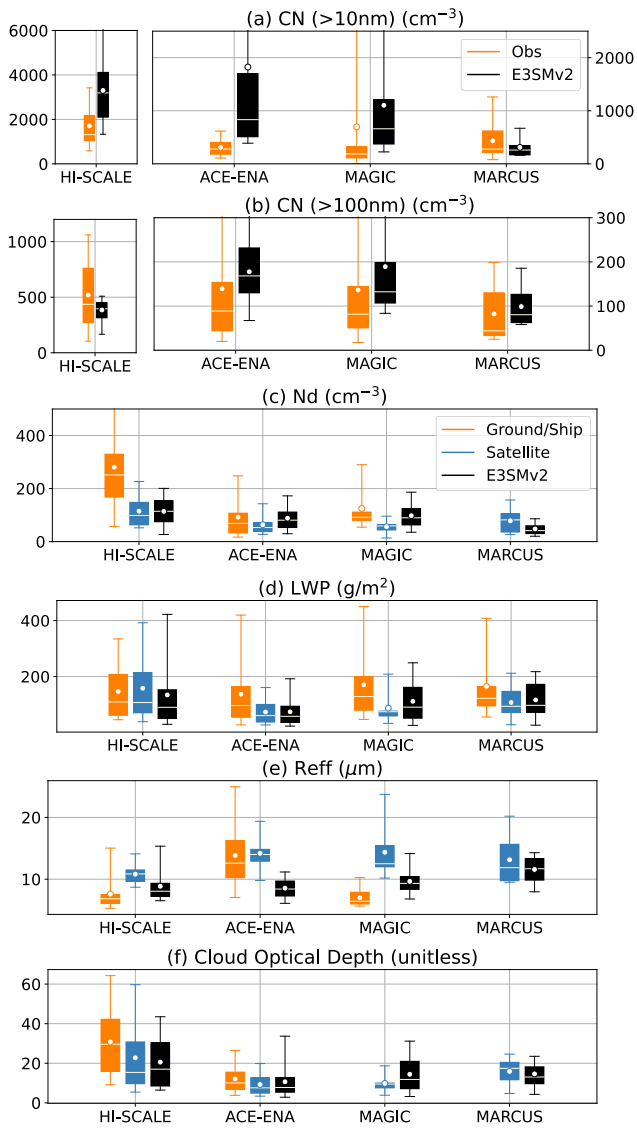
380



381
 382 Figure 6: Box-whisker plots of (a) CN for size > 10 nm, (b) CN for size > 100 nm, (c) in-
 383 cloud N_d , (d) LWC for all data from aircraft field campaigns at CUS, ENA, NEP and SO
 384 regions from left to right. Boxes denote 25th and 75th percentiles, whiskers denote 5th and
 385 95th percentiles, the white horizontal line represents median values, and the white dot
 386 represents mean values. For aerosol number concentrations, the y axes for HI-SCALE are
 387 separated from other field campaigns for better visualization. The top whiskers that are
 388 out of the y-axis range are: (a) HI-SCALE obs: 13681. ACE-ENA E3SMv2: 2061.
 389 SOCRATES obs: 2745. (b): ACE-ENA E3SMv2: 304. CSET obs: 305. CSET E3SMv2:
 390 400. (c): HI-SCALE obs: 397.



391

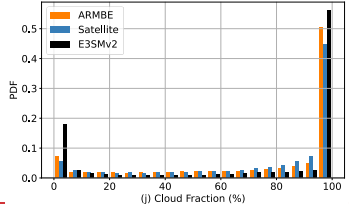
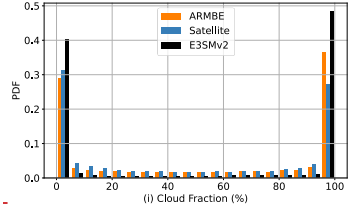
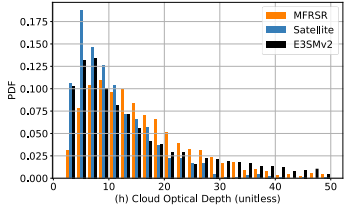
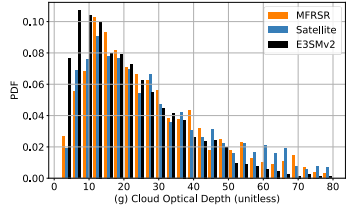
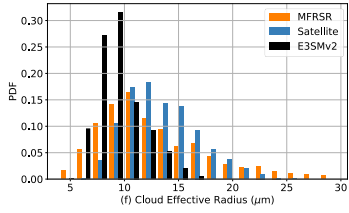
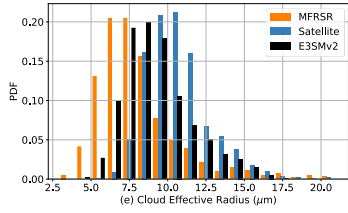
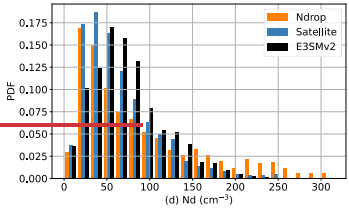
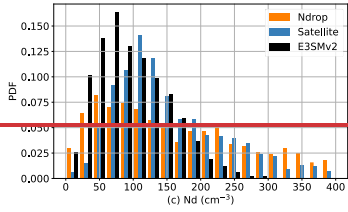
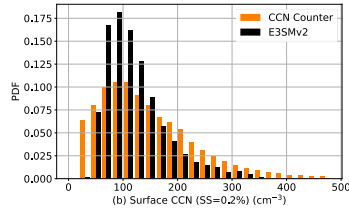
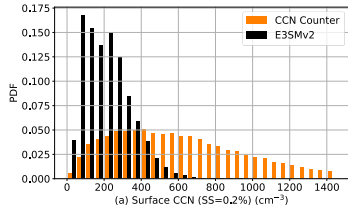


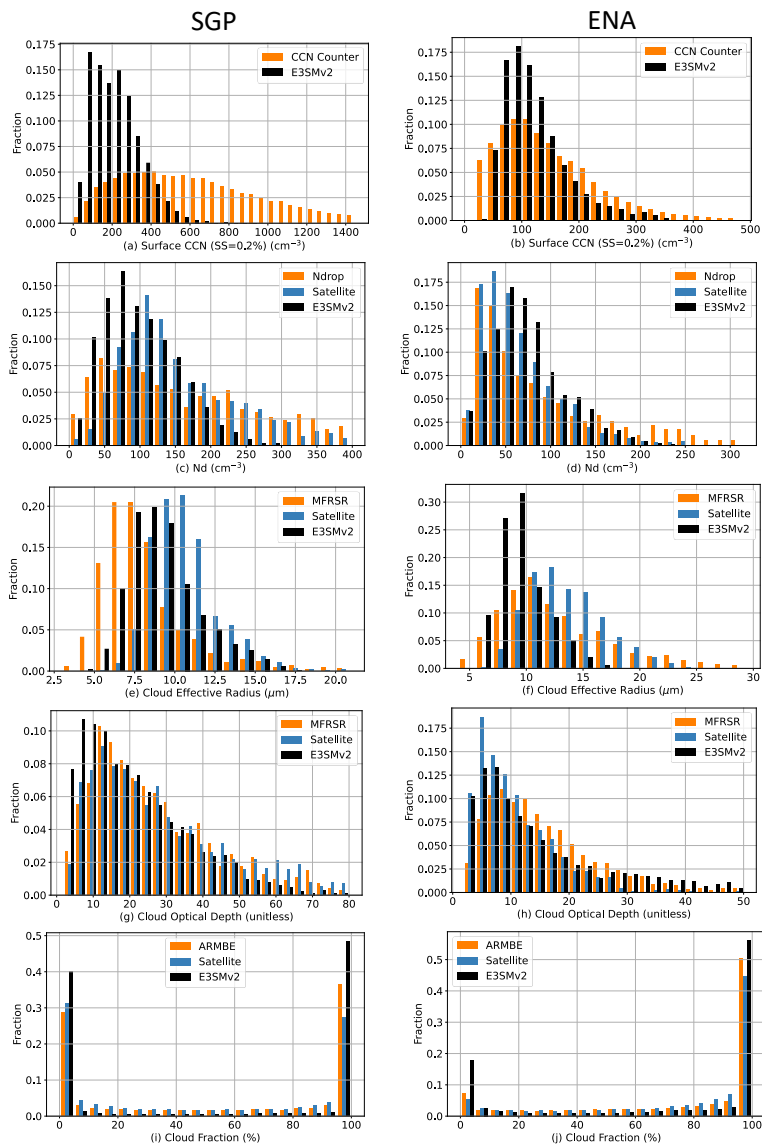
392
 393 Figure 7: Box-whisker plots of (a) CN for size > 10 nm, (b) CN for size > 100 nm, (c)
 394 layer-mean N_d , (d) LWP, (e) R_{eff} , (f) cloud optical depth for overcast low-level liquid
 395 cloud conditions (cloud top height < 4 km, cloud fraction > 90% and ice water path < 0.01
 396 mm) in ground and ship field campaigns at CUS, ENA, NEP and SO regions from left to
 397 right. Boxes denote 25th and 75th percentiles, whiskers denote 5th and 95th percentiles, the

398 white horizontal line represents median values, and the white dot represents mean values.
399 For aerosol number concentrations, the y axes for HI-SCALE are separated from other
400 field campaigns for better visualization. The top whiskers that are out of the y-axis range
401 are: (a) HI-SCALE E3SMv2: 6102. ACE-ENA E3SMv2: 7575. MAGIC obs: 3330. MAGIC
402 E3SMv2: 3771. (b): ACE-ENA obs: 304.7. ACE-ENA E3SMv2: 328.3. MAGIC obs: 377.7.
403 MAGIC E3SMv2: 577.8. (c): HI-SCALE obs: 670.9.

SGP

ENA



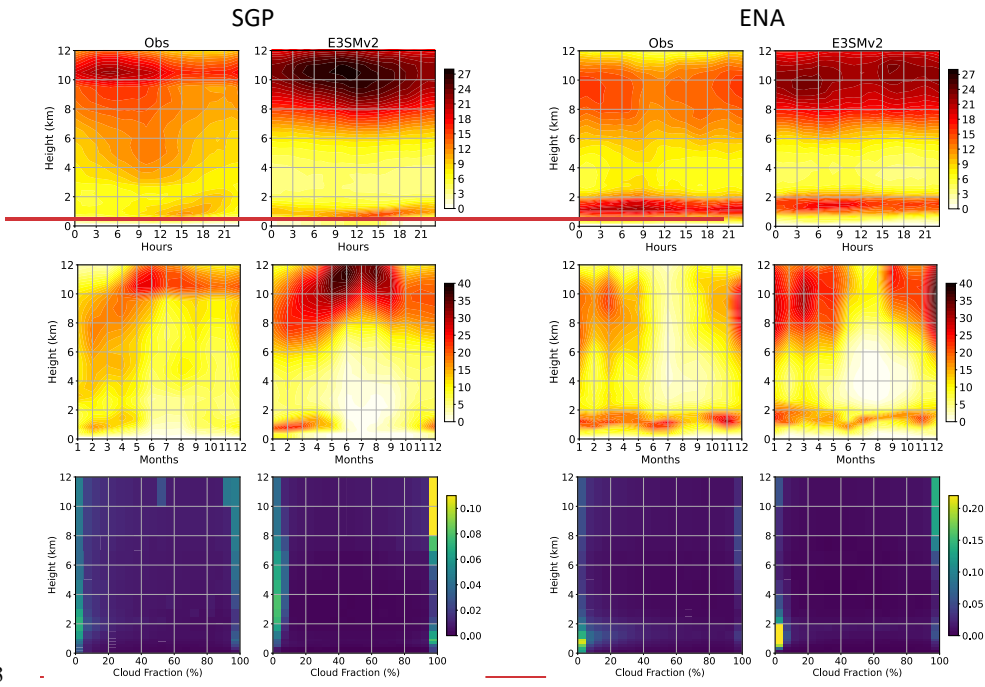


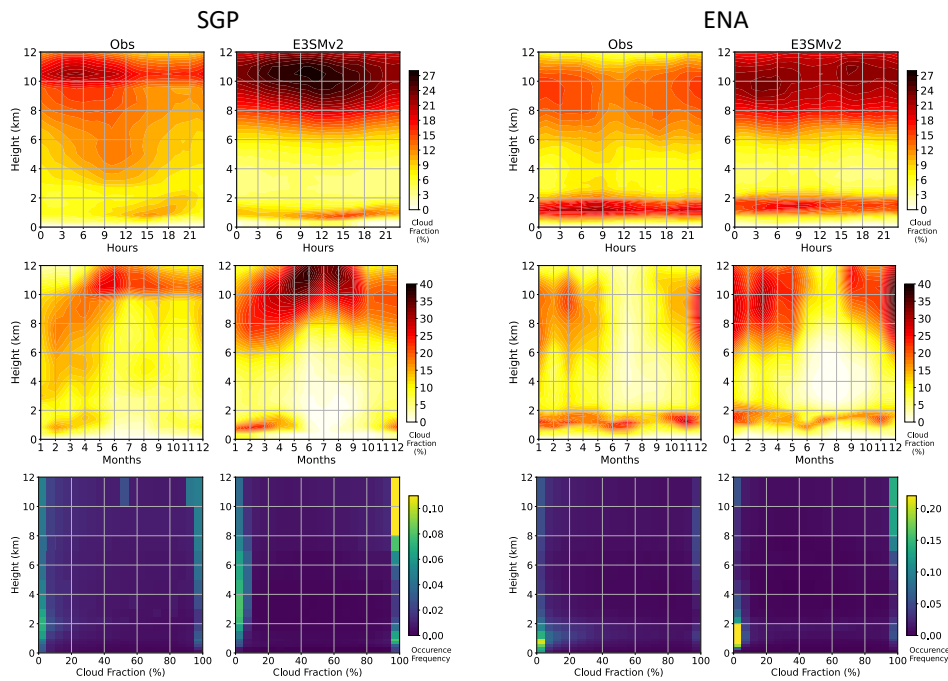
405

406 Figure 8: histogram of (from top to bottom) surface CCN number concentration, layer-
 407 mean N_d , R_{eff} , cloud optical depth and total cloud fraction at (left) SGP from 2011 to
 408 2020 and (right) ENA from 2016 to 2018. Surface CCN and total cloud fraction are using
 409 all-condition samples while N_d , R_{eff} , cloud optical depth data are filtered for overcast

410 low-level liquid clouds (cloud top height < 4 km, cloud fraction > 90%, ice water path <
411 0.01 mm).

412 Figure 8 shows [PDFs-histograms](#) of surface CCN number concentration in 0.2% supersaturation, cloud
413 layer mean N_d , R_{eff} , cloud optical depth and total cloud fraction for long-term diagnostics at SGP (year
414 2011-2020) and ENA (year 2016-2018) sites. E3SMv2 fails to reproduce the long tail of large values in
415 CCN and N_d , especially over SGP. This is consistent with the underestimation of CN (> 100 nm) during
416 the HI-SCALE field campaign shown in Figures 6 and 7. Compared with ground retrievals, E3SMv2
417 R_{eff} is larger at SGP but smaller at ENA. However, satellite-retrieved R_{eff} has larger values than
418 E3SMv2 at SGP. As discussed before, discrepancies between satellite and ground retrievals can be
419 substantial for some locations and variables, and considering both in evaluating model performance gives
420 a sense for how uncertain comparisons are. E3SMv2 generally captures the [PDFs-histograms](#) of cloud
421 optical depth and total cloud fraction, although it underestimates the frequency of partial-cloudy
422 conditions and overestimates the frequency of clear-sky and overcast conditions.





424
 425 Figure 9: (top) Diurnal cycle, (middle) seasonal cycle, and (bottom) occurrence frequency
 426 of vertical cloud fraction at (left) SGP from 2011 to 2020 and (right) ENA from 2016 to
 427 2018.

428 Figure 9 shows the long-term diagnostics of mean diurnal cycles, seasonal cycles and ~~PDFs-histograms~~
 429 cloud fraction by height at SGP and ENA sites. Overall, the mean fraction of high clouds is looks
 430 overestimated in E3SMv2. This overestimation Similar results has been reported in many previous studies
 431 in the Community Earth System Model (CESM)-E3SM model family (e.g., Song et al., 2012; Cheng and
 432 Xu, 2013; Xu and Cheng, 2013b, a; Tang et al., 2016; Zhang et al., 2020). However, this is not an apple-
 433 to-apple comparison, as cloud fraction in ESMs includes clouds that are optically very thin that cannot be
 434 detected by satellite passive sensors or cloud radars. When satellite simulators are used, slight
 435 underestimation of high cloud fraction by E3SM is seen over most tropical deep convection regions. The
 436 comparison of high cloud fraction from simulators with the corresponding satellite observations showed
 437 that E3SM slightly underestimates high clouds over most tropical deep convection regions (Zhang et al.,
 438 2019; Xie et al., 2018; Rasch et al., 2019). Unfortunately, ground-based radar simulator of our model does
 439 not output cloud vertical profiles from satellite simulators is not available in the current model, which
 440 prevents a direct apple-to-apple comparison. Thus, caution should be taken when comparing magnitude of
 441 cloud fraction from direct model output and radar measurements direct model output is used to compare
 442 with observed cloud fraction. Here we focus on the temporal variabilities (diurnal and seasonal cycles)

Field Code Changed

Field Code Changed

443 [and the occurrence frequency distribution of cloud fraction, which are less relevant to the detection](#)
444 [threshold of cloud radars.](#)

445 At SGP, observations show formation of low clouds in the afternoon and in late winter through
446 springtime. High clouds peak overnight into the early morning and in the spring to summer,
447 corresponding to nocturnal deep convective systems common over SGP (Tang et al., 2022b; Tang et al.,
448 2021; Jiang et al., 2006). These features are reasonably well represented in E3SMv2, although low-level
449 cloud deepening in the afternoon is not well predicted, and high-level clouds peak in the late rather than
450 early morning. At ENA, marine stratus or stratocumulus clouds occur in any month and at any time of the
451 day, but with less frequency in late summer and in afternoon. High clouds are more frequent in winter
452 months than in summer months and occur throughout the diurnal cycle with a slight mid-day minimum.
453 These features are well captured by E3SMv2. At both sites, high clouds usually occur with high fraction
454 (> 95%) while low clouds are more likely associated with small fraction (< 5%) (bottom row). At SGP,
455 high occurrence of low cloud fraction extends vertically up to the tropopause, representing frequently
456 occurring deep convection. At ENA, low clouds have less vertical extension but are more likely to expand
457 to greater fraction. E3SMv2 reproduces these cloud features in occurrence frequency, ~~with overestimation~~
458 ~~of occurrence frequency in high (>95%) and low (<5%) cloud fraction consistent with Figure 8.~~

459 ~~Overall, the mean fraction of high clouds is overestimated in E3SMv2. This overestimation has been~~
460 ~~reported in many previous studies in the Community Earth System Model (CESM) E3SM model family~~
461 ~~(e.g., Song et al., 2012; Cheng and Xu, 2013; Xu and Cheng, 2013b, a; Tang et al., 2016; Zhang et al.,~~
462 ~~2020). However, this is not an apple to apple comparison, as cloud fraction in ESMs includes clouds that~~
463 ~~are optically very thin that cannot be detected by satellite passive sensors or cloud radar. When satellite~~
464 ~~simulators are used, slight underestimation of high cloud fraction by E3SM is seen over most tropical~~
465 ~~deep convection regions (Zhang et al., 2019; Xie et al., 2018; Rasch et al., 2019). Unfortunately, our~~
466 ~~model does not output cloud vertical profiles from satellite simulators, which prevents a direct apple to~~
467 ~~apple comparison. Thus, caution should be taken when direct model output is used to compare with~~
468 ~~observed cloud fraction.~~

469 5.2. Multi-variable relationships related to ACI

470 The effective radiative forcing due to ACI processes are complex, nonlinear, and highly uncertain despite
471 their significant impact on climate. ACI studies are usually conducted by examining relationships
472 between aerosols, clouds, and radiation variables that are known to interact with one another. Given so
473 many variable combinations related to ACI, ESMAC Diags v2 provides a framework for users to examine
474 relationships between the variables they choose with joint histograms, scatter plots and heatmaps. Here
475 we show a few examples to assess relationships between CCN, N_d , LWP, and top of atmosphere (TOA)
476 albedo. [ESMAC Diags v2 calculate layer-mean \$N_d\$ from three sources: integrated vertically from native](#)
477 [model output, retrieved using Ndrop algorithm and using Nd_sat algorithm, as shown in Table 3. In this](#)
478 [study we only show the ACI diagnostics using native model output, as it reveals the “true” ACI relations](#)
479 [in the model. Users can choose to use the retrieved \$N_d\$ in their studies for their purposes.](#)

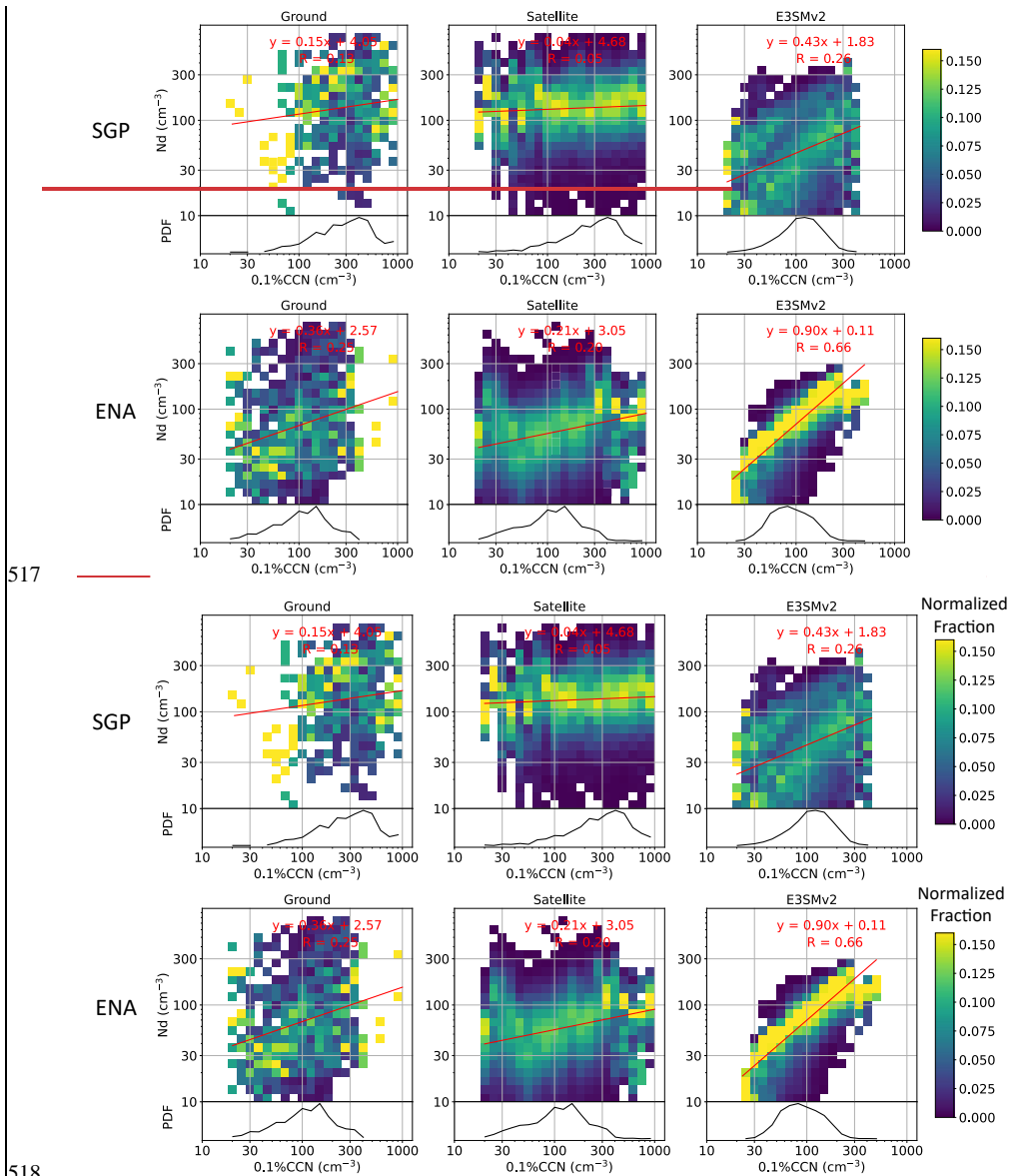
480 The dependence of TOA albedo on CCN number concentration for stratiform warm clouds can be
481 decomposed (e.g., following Quaas et al. (2008)) as:

482

$$\frac{dA}{d\ln CCN} = \left(\frac{\partial A}{\partial \ln N_d} + \frac{\partial A}{\partial \ln LWP} \frac{d\ln LWP}{d\ln N_d} \right) \frac{d\ln N_d}{d\ln CCN} \quad (1)$$

483 which allows isolation of “Twomey effect” $\left(\frac{\partial A}{\partial \ln N_d}\right) \left(\frac{d\ln N_d}{d\ln CCN}\right)$ and “LWP adjustment” $\left(\frac{\partial A}{\partial \ln LWP}\right) \left(\frac{d\ln LWP}{d\ln N_d}\right)$ associated
 484 with specific ACI processes. Here we use joint histograms and heatmaps to evaluate each component,
 485 $\frac{d\ln N_d}{d\ln CCN}$, $\frac{d\ln LWP}{d\ln N_d}$, $\frac{\partial A}{\partial \ln N_d}$ and $\frac{\partial A}{\partial \ln LWP}$ based on long-term ground and satellite measurements at SGP (2011-
 486 2020) and ENA (2016-2018) sites. The analysis in this section (except Figure 11) is limited to overcast
 487 (cloud fraction > 90%), low-level (cloud top height < 4 km) liquid (ice water path < 0.01 mm) clouds.
 488 Since there is no direct measurement of cloud base CCN concentration from remote sensors, surface CCN
 489 concentration is used in this study and only clouds that are most likely to be affected by surface
 490 conditions are examined. These clouds are identified as having cloud base potential temperature minus
 491 surface potential temperature smaller than 2 K. For satellite measurements, samples with solar zenith
 492 angle greater than 65° are removed to avoid N_d retrieval biases (Grosvenor et al., 2018). The sample
 493 number of (ground, satellite, E3SM) for overcast low-level liquid clouds are (1766, 1217, 6369) at SGP
 494 and (3450, 1345, 2884) at ENA, respectively. To increase sample size for more robust statistics, satellite
 495 retrievals and E3SM outputs over a 5°×5° domain centered on SGP and ENA sites are included. This
 496 increases the sample number to (1766, 71942, 15231) at SGP and (3450, 104260, 28184) at ENA.
 497 Analyses of all-sky conditions and overcast low-level liquid clouds for a single grid point over each site
 498 are shown in Figures S2-S7 in the supplementary material. Increasing sample domain for satellite and
 499 E3SM data does not change the over~~all~~ statistics shown here.

500 The change of N_d in response to a change of surface CCN number concentration $\left(\frac{d\ln N_d}{d\ln CCN}\right)$ is heavily
 501 influenced by processes such as aerosol activation. Figure 10 shows the joint [probability density function](#)
 502 [\(PDF\)](#)PDFs of N_d and surface CCN number concentration at 0.1% supersaturation normalized within
 503 each CCN bin. Ground and satellite observations show similar linear fit of $\ln N_d - \ln CCN$ relation,
 504 although ground-based plots have much smaller sample number. E3SMv2 shows more sensitive $N_d -$
 505 CCN relationships than observations at both SGP and ENA sites, with the relationship tighter at ENA and
 506 more scattered at SGP. As a cross validation, Figure 11 shows the $N_d -$ CCN relationships from short-
 507 term aircraft campaign during HI-SCALE and ACE-ENA. The comparison with in-situ aircraft
 508 measurements confirms that E3SMv2 has more sensitive N_d to CCN [relationship](#) than observations.
 509 These results indicate that aerosol activation in E3SMv2 may be too weak in low CCN conditions and too
 510 strong in high CCN conditions, which may be related to the differences in simulated and observed updraft
 511 velocity and supersaturation (Varble et al., 2023). Note that E3SMv2 produces a significant number of
 512 small N_d (< 20 cm⁻³) samples (Figure 11). This feature is reported in Golaz et al. (2022) and is partially
 513 removed by setting a minimum threshold of $N_d = 10$ cm⁻³. However, as seen in Figure 11, there are still a
 514 large number of N_d between 10 and 20 cm⁻³. Further investigation is underway to diagnose the causes of
 515 the abundant low- N_d values. The diagnostics shown here indicate that a more physical method should be
 516 applied to improve the simulated N_d .

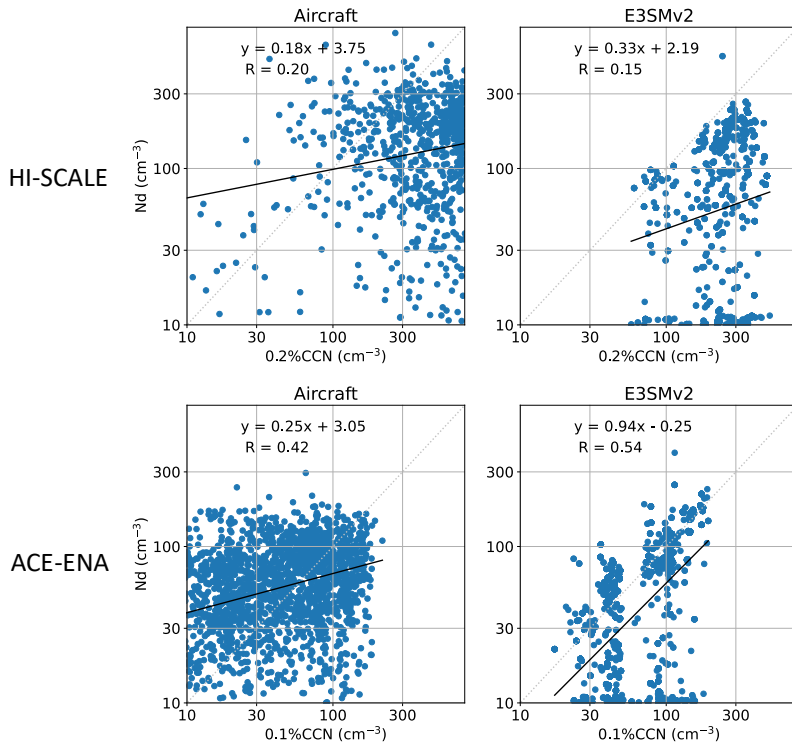


517

518

519 Figure 10: Joint histogram of layer-mean N_d versus surface CCN number concentration at
 520 0.1% supersaturation, normalized within each CCN number concentration bin (PDF of
 521 CCN shown in the bottom of each panel). Samples are constrained to likely surface-

522 coupled, overcast low-level liquid clouds (cloud top height < 4 km, cloud fraction > 90%,
 523 ice water path < 0.01 mm and potential temperature difference between cloud base and
 524 surface < 2 K). Available samples within a $5^\circ \times 5^\circ$ region centered on SGP (top) and ENA
 525 (bottom) for satellite and E3SMv2 datasets are included. Linear fits and R values are
 526 shown in red.



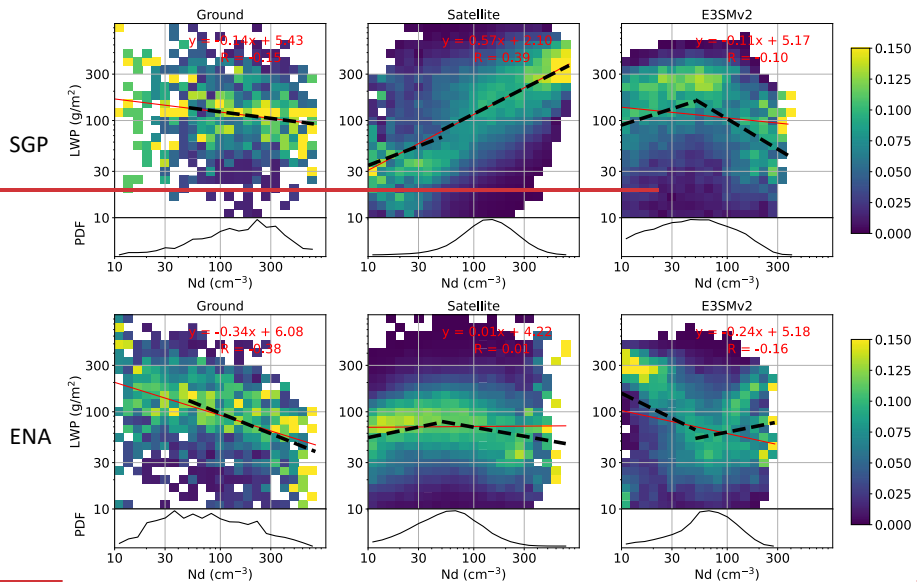
527
 528 Figure 11: Scatter plots for N_d versus CCN along the flight tracks from (top) HI-SCALE
 529 and (bottom) ACE-ENA campaigns. Note that CCN number concentration measurements
 530 are taken under $\sim 0.2\%$ supersaturation for HI-SCALE and under $\sim 0.1\%$ supersaturation for
 531 ACE-ENA. Linear fits and R values are shown in each panel. $R = 0.34$ (SGP) and 0.74
 532 (ENA) for E3SMv2 if a minimum $N_d = 20 \text{ cm}^{-3}$ is applied.

533
 534 The term $\frac{d \ln LWP}{d \ln N_d}$ is commonly interpreted as the response of LWP to a perturbation in N_d tied to
 535 suppression of precipitation (increase LWP) or enhancement of evaporation (decrease LWP) (e.g.,
 536 Glassmeier et al., 2019). Gryspeerd et al. (2019) show that the satellite retrieved LWP over ocean
 537 increases with N_d when $N_d < \sim 30 \text{ cm}^{-3}$ and decreases when $N_d > \sim 30 \text{ cm}^{-3}$. This relation is also seen

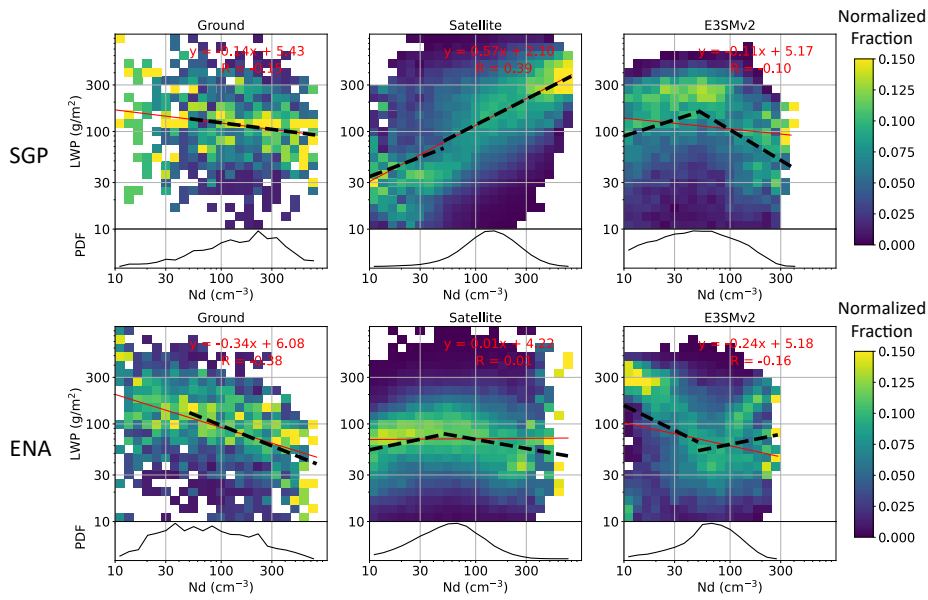
538 in satellite retrievals at ENA (Figure 12) when using a higher threshold $N_d = 50 \text{ cm}^{-3}$ to perform linear
539 fits (black dashed lines). The linear fit is insignificant for $N_d < 50 \text{ cm}^{-3}$ in surface retrievals at both
540 sites, partly due to small sample number, and also potentially related to drizzle contamination of LWP.
541 The slope of the LWP – N_d relation in satellite retrievals at SGP is positive for both N_d ranges. This is
542 opposed to slope shown in the ground retrievals and indicates that retrieval biases may cause opposite
543 results in ACI studies. The reason why satellite retrievals show positive LWP – N_d relation at SGP is
544 subject to further investigation.

545 The E3SMv2 simulated LWP – N_d relation is quite different from satellite retrievals at both sites. At
546 SGP, it generates a positive slope for $N_d < 50 \text{ cm}^{-3}$, and a negative slope for $N_d > 50 \text{ cm}^{-3}$. At ENA, it
547 shows an opposite relation, with LWP decreases for small N_d and increases for large N_d . We examined a
548 few other oceanic regions with frequent stratus or stratocumulus clouds in E3SMv2 and saw similar
549 behavior (not shown). However, LWP – N_d relation in E3SMv1 performs quite differently, as shown in
550 Varble et al. (2023). The causes of the different LWP – N_d relation behaviors in E3SM are under further
551 investigation. Varble et al. (2023) discussed potential physical mechanisms that may affect the different
552 LWP responses to N_d in observation and simulation, such as different atmospheric states in E3SM and
553 observations. Our user-friendly diagnostics package allows these analyses to be routinely performed for
554 the purpose of better understanding critical model behaviors at process- and mechanistic-levels, providing
555 observational constraints to facilitate model development efforts.

556

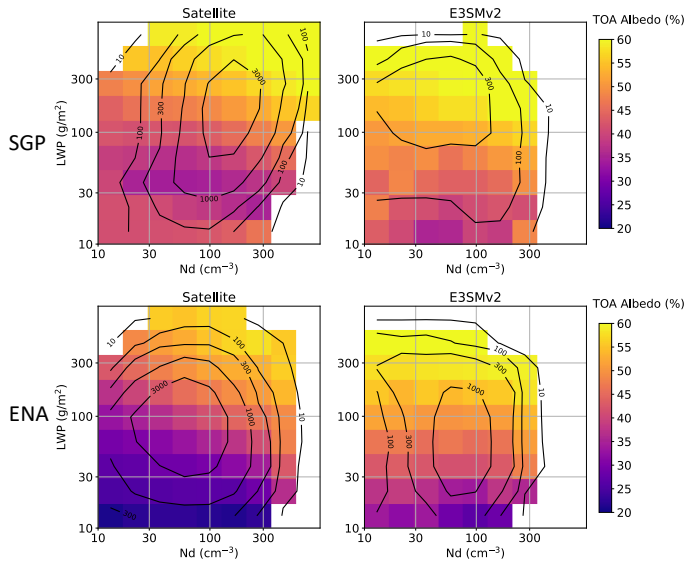


557



558 Figure 12: Following Figure 10, but for the N_d bin-normalized joint histogram of LWP
 559 versus N_d . Red lines and equations are linear fits for all data samples and black dashed

560 lines are linear fits for $N_d < 50 \text{ cm}^{-3}$ and $N_d > 50 \text{ cm}^{-3}$ when the fits are statistically
 561 significant ($p < 0.01$).



562
 563 Figure 13: Heatmaps of mean TOA albedo versus LWP and N_d for likely surface-coupled,
 564 overcast low-level liquid clouds (cloud top height $< 4 \text{ km}$, cloud fraction $> 90\%$, ice water
 565 path $< 0.01 \text{ mm}$ and potential temperature difference between cloud base and surface < 2
 566 K). Data include samples within a $5^\circ \times 5^\circ$ region centered on SGP (top) and ENA (bottom).
 567 Valid sample number is shown in black contour lines. Grids with valid sample number $<$
 568 10 are not filled. Ground data is not included, since the TOA albedo is not available.

569 Figure 13 shows heatmaps of mean TOA albedo with respect to LWP and N_d from which $\frac{\partial A}{\partial \ln N_d}$ and
 570 $\frac{\partial A}{\partial \ln LWP}$ can be derived. At both ENA and SGP, TOA albedo generally increases with increases of LWP
 571 and N_d , except at SGP when LWP is small. The increasing albedo in small LWP may be due to retrieval
 572 artifact as uncertainty becomes large when LWP is small (e.g., $< 20 \text{ g/m}^2$), solar zenith angle is large
 573 (e.g., $> 55^\circ$), or cloud optical depth is small (e.g., < 5) (Grosvenor et al., 2018). In most LWP- N_d bins,
 574 TOA albedo at SGP is generally higher than at ENA, which is expected for clouds with smaller droplet
 575 sizes. Increasing TOA albedo with increases of LWP is also seen in E3SMv2, but the dependence with N_d
 576 is weak. This can be impacted by correlation between solar zenith angle and N_d in E3SM simulation, as
 577 discussed in Varble et al. (2023). For a given LWP and N_d , TOA albedo is generally higher in E3SMv2
 578 than in satellite observations, indicating that shallow clouds may be too reflective in the model, possibly
 579 due to smaller cloud R_{eff} (Figure 8).

580 The above illustration of single-variable and multi-variable diagnostics present examples to demonstrate
 581 the capability of ESMAC Diags v2. More analyses, such as selecting other variables, performing

582 additional data filtering or treatments, and examining ACI relationships with other variable combinations,
583 can be conducted through user-specified settings. A detailed user guide and a collection of example
584 scripts are included in the diagnostics package to assist users design customized diagnostics suited to their
585 specific needs.

586 5. Summary

587 We developed ~~an~~the Earth System Model aerosol-cloud diagnostics package (ESMAC Diags) to
588 facilitate routine evaluation of aerosols, clouds and ACI in the U.S. DOE's E3SM model using multiple
589 platforms of observations. As an updated version of ESMAC Diags v1 (Tang et al., 2022a) which mainly
590 focuses on aerosol properties, this paper described ESMAC Diags v2 that focuses on both aerosols,
591 clouds, as well as their interactions. In addition to the short-term field campaigns included in ESMAC
592 Diags v1, long-term diagnostics from two permanent ARM sites (SGP and ENA, each represents
593 continental and maritime conditions, respectively) are now conducted to provide more robust evaluation.
594 The newly added multi-variable joint histograms, scatter plots and heatmaps allow users to examine
595 correlations between variables that are relevant to the study of ACI.

596 Ground- and ship-based aerosol measurements are frequently impacted by local-scale emissions sources
597 such as those from airport or ship exhaust. These local sources are not resolved by coarse-resolution
598 ESMs, which usually represent an environment averaged within a region of tens to hundreds of kilometers
599 in size. In ESMAC Diags, we used available contamination-removed aerosol data, such as those from
600 Gallo et al. (2020) for ENA, and Humphries (2020) for MARCUS, and applied data filtering for other
601 field campaigns. The observations are harmonized into a uniform data format and temporal resolution that
602 are comparable with ESMs. Aircraft measurements retain higher resolution (currently 1-min) to preserve
603 high spatiotemporal variability, although ESMs have to be downscaled for evaluation with aircraft
604 measurements. This limitation of scale mismatch must be accepted to perform evaluation in current
605 coarse-resolution ESMs. Nevertheless, as ESM grid spacing approaches a few kilometers via regional
606 refinement (Tang et al., 2019) or global convection-permitting configuration (Caldwell et al., 2021), the
607 scale inconsistency between models and observations is reduced. ESMAC Diags can easily adjust the
608 preprocessing output resolution to facilitate the evaluation of high-resolution model output.

609 Cloud microphysical properties heavily rely on remote sensing measurements to achieve more robust
610 sampling, with imperfect retrieval algorithms needed to estimate these variables. Microphysical retrievals
611 are more uncertain than typical atmospheric state measurements due to the need for many assumptions
612 related to cloud dynamical and physical processes. We have shown (in Section 3) that ground- and
613 satellite-based retrievals of N_d and R_{eff} are overall consistent with each other and with in-situ aircraft
614 measurements, with some systematic differences such as smaller N_d and larger R_{eff} in satellite retrievals.
615 The discrepancies between different retrievals can be larger for individual days (e.g., Figure S1) but can
616 be mitigated to some degrees when considering broader statistics (Figures 3 and 4). The usage of multiple
617 retrieval datasets is critical to understand the robustness of evaluation results, as the spread between
618 different datasets indicates how robust model-observation differences are and guides interpretations of
619 model biases to support model development.

620 Finally, this paper presents a few examples of how well E3SMv2 simulates aerosols, clouds and ACI. We
621 showed that ESMAC Diags can be used to target further investigation into specific parameterization
622 components. For example, the analysis of N_d – CCN correlation indicates that E3SMv2 may exhibit too

623 weak aerosol activation in low CCN conditions and too strong in high CCN conditions; the analysis of
624 LWP – N_d correlation indicates that either the precipitation suppression and cloud evaporation
625 mechanisms are not well represented, or there are other mechanisms dominating LWP – N_d correlation in
626 E3SMv2. These diagnostic analyses provide insights into areas in aerosols, clouds and ACI that warrant
627 special attention in future model development efforts. As ESMs continuously improve its physical
628 parameterizations, resolution, and numerical schemes, ESMAC Diags offers a valuable tool for
629 systematically evaluating the performance of the newer versions of a model in simulating aerosol, clouds
630 and ACI.

631 **Code availability:**

632 *The current version of ESMAC Diags is publicly available through GitHub ([https://github.com/eagles-](https://github.com/eagles-project/ESMAC_diags)*
633 *[project/ESMAC_diags](https://github.com/eagles-project/ESMAC_diags)) under the new BSD license. The exact version (2.1.2) of the code used to produce*
634 *the results used in this paper is archived on Zenodo (<https://doi.org/10.5281/zenodo.7696871>). The model*
635 *simulation used in this paper is version 2.0 (<https://doi.org/10.11578/E3SM/dc.20210927.1>) of E3SM.*

636 **Data availability:**

637 *Measurements from the HI-SCALE, ACE-ENA, MAGIC, and MARCUS campaigns as well as the SGP*
638 *and ENA sites are supported by the DOE Atmospheric Radiation Measurement (ARM) user facility and*
639 *available at <https://adc.arm.gov/discovery/>. Measurements from the CSET and SOCRATES campaigns*
640 *are supported by National Science Foundation (NSF) and obtained from NCAR Earth Observing*
641 *Laboratory at https://data.eol.ucar.edu/master_lists/generated/cset/ and*
642 *https://data.eol.ucar.edu/master_lists/generated/socrates/, respectively. DOI numbers or references of*
643 *individual datasets are given in Tables S1-S8. All the preprocessed observational and model data used to*
644 *produce the results used in this paper is archived on Zenodo (<https://doi.org/10.5281/zenodo.7478657>).*

645 **Author contribution:**

646 *ST, JDF and PM designed the diagnostics package; ST and ACV wrote the code and performed the*
647 *analysis; PW, XD, FM and MP processed the field campaign datasets and provided discussions on the*
648 *data quality issues; KZ contributed to the model simulation; JCH contributed to the package design and*
649 *setup; ST wrote the original manuscript; all authors reviewed and edited the manuscript.*

650 **Competing interests:**

651 *Po-Lun Ma is a Topical Editor of Geoscientific Model Development. Other authors declare that they have*
652 *no conflict of interest.*

653 **Acknowledgements:**

654 *This study was supported by the Enabling Aerosol-cloud interactions at GLocal convection-permitting*
655 *scalES (EAGLES) project (74358), funded by the U.S. Department of Energy, Office of Science, Office of*
656 *Biological and Environmental Research, Earth System Model Development (ESMD) program area. We*
657 *thank the numerous instrument mentors for providing the data. This research used resources of the*
658 *National Energy Research Scientific Computing Center (NERSC), a U.S. Department of Energy Office of*
659 *Science User Facility operated under Contract No. DE-AC02-05CH11231, using NERSC awards ALCC-*
660 *ERCAP0016315, BER-ERCAP0015329, BER-ERCAP0018473, and BER-ERCAP0020990. Pacific*
661 *Northwest National Laboratory (PNNL) is operated for DOE by Battelle Memorial Institute under*
662 *contract DE-AC05-76RL01830.*

663

664 **References:**

- 665 Albrecht, B., Ghate, V., Mohrmann, J., Wood, R., Zuidema, P., Bretherton, C., Schwartz, C., Eloranta, E.,
666 Glienke, S., Donaher, S., Sarkar, M., McGibbon, J., Nugent, A. D., Shaw, R. A., Fugal, J., Minnis, P.,
667 Paliknoda, R., Lussier, L., Jensen, J., Vivekanandan, J., Ellis, S., Tsai, P., Rilling, R., Haggerty, J., Campos, T.,
668 Stell, M., Reeves, M., Beaton, S., Allison, J., Stossmeister, G., Hall, S., and Schmidt, S.: Cloud System
669 Evolution in the Trades (CSET): Following the Evolution of Boundary Layer Cloud Systems with the NSF–
670 NCAR GV, *Bull. Amer. Meteor. Soc.*, 100, 93-121, <https://doi.org/10.1175/bams-d-17-0180.1>, 2019.
671 AMWG Diagnostic Package: [https://www.cesm.ucar.edu/working_groups/Atmosphere/amwg-
672 diagnostics-package/](https://www.cesm.ucar.edu/working_groups/Atmosphere/amwg-diagnostics-package/), last access: 2 November 2021. 2021.
673 Bennartz, R.: Global assessment of marine boundary layer cloud droplet number concentration from
674 satellite, *Journal of Geophysical Research: Atmospheres*, 112, <https://doi.org/10.1029/2006JD007547>,
675 2007.
676 Caldwell, P. M., Terai, C. R., Hillman, B., Keen, N. D., Bogenschutz, P., Lin, W., Beydoun, H., Taylor, M.,
677 Bertagna, L., Bradley, A. M., Clevenger, T. C., Donahue, A. S., Eldred, C., Foucar, J., Golaz, J.-C., Guba, O.,
678 Jacob, R., Johnson, J., Krishna, J., Liu, W., Pressel, K., Salinger, A. G., Singh, B., Steyer, A., Ullrich, P., Wu,
679 D., Yuan, X., Shpund, J., Ma, H.-Y., and Zender, C. S.: Convection-Permitting Simulations With the E3SM
680 Global Atmosphere Model, *Journal of Advances in Modeling Earth Systems*, 13, e2021MS002544,
681 <https://doi.org/10.1029/2021MS002544>, 2021.
682 Cheng, A. and Xu, K.-M.: Evaluating Low-Cloud Simulation from an Upgraded Multiscale Modeling
683 Framework Model. Part III: Tropical and Subtropical Cloud Transitions over the Northern Pacific, *J.*
684 *Climate*, 26, 5761-5781, <https://doi.org/10.1175/JCLI-D-12-00650.1>, 2013.
685 Choudhury, G. and Tesche, M.: Estimating cloud condensation nuclei concentrations from CALIPSO lidar
686 measurements, *Atmos. Meas. Tech.*, 15, 639-654, <https://doi.org/10.5194/amt-15-639-2022>, 2022.
687 E3SM Diagnostics: <https://e3sm.org/resources/tools/diagnostic-tools/e3sm-diagnostics/>, last access: 2
688 November 2021. 2021.
689 Eyring, V., Righi, M., Lauer, A., Evaldsson, M., Wenzel, S., Jones, C., Anav, A., Andrews, O., Cionni, I.,
690 Davin, E. L., Deser, C., Ehbrecht, C., Friedlingstein, P., Gleckler, P., Gottschaldt, K. D., Hagemann, S.,
691 Jukes, M., Kindermann, S., Krasting, J., Kunert, D., Levine, R., Loew, A., Mäkelä, J., Martin, G., Mason, E.,
692 Phillips, A. S., Read, S., Rio, C., Roehrig, R., Senftleben, D., Sterl, A., van Ulft, L. H., Walton, J., Wang, S.,
693 and Williams, K. D.: ESMValTool (v1.0) – a community diagnostic and performance metrics tool for
694 routine evaluation of Earth system models in CMIP, *Geosci. Model Dev.*, 9, 1747-1802,
695 <https://doi.org/10.5194/gmd-9-1747-2016>, 2016.
696 Fast, J. D., Berg, L. K., Alexander, L., Bell, D., D'Ambro, E., Hubbe, J., Kuang, C., Liu, J., Long, C., Matthews,
697 A., Mei, F., Newsom, R., Pekour, M., Pinterich, T., Schmid, B., Schobesberger, S., Shilling, J., Smith, J. N.,
698 Springston, S., Suski, K., Thornton, J. A., Tomlinson, J., Wang, J., Xiao, H., and Zelenyuk, A.: Overview of
699 the HI-SCALE Field Campaign: A New Perspective on Shallow Convective Clouds, *Bull. Amer. Meteor.*
700 *Soc.*, 100, 821-840, <https://doi.org/10.1175/bams-d-18-0030.1>, 2019.
701 Gallo, F., Uin, J., Springston, S., Wang, J., Zheng, G., Kuang, C., Wood, R., Azevedo, E. B., McComiskey, A.,
702 Mei, F., Theisen, A., Kyrouac, J., and Aiken, A. C.: Identifying a regional aerosol baseline in the eastern
703 North Atlantic using collocated measurements and a mathematical algorithm to mask high-submicron-
704 number-concentration aerosol events, *Atmos. Chem. Phys.*, 20, 7553-7573,
705 <https://doi.org/10.5194/acp-20-7553-2020>, 2020.
706 Gelaro, R., McCarty, W., Suarez, M. J., Todling, R., Molod, A., Takacs, L., Randles, C., Darmenov, A.,
707 Bosilovich, M. G., Reichle, R., Wargan, K., Coy, L., Cullather, R., Draper, C., Akella, S., Buchard, V., Conaty,
708 A., da Silva, A., Gu, W., Kim, G. K., Koster, R., Lucchesi, R., Merkova, D., Nielsen, J. E., Partyka, G.,
709 Pawson, S., Putman, W., Rienecker, M., Schubert, S. D., Sienkiewicz, M., and Zhao, B.: The Modern-Era

710 Retrospective Analysis for Research and Applications, Version 2 (MERRA-2), *J. Climate*, 30, 5419-5454,
711 <https://doi.org/10.1175/JCLI-D-16-0758.1>, 2017.

712 Glassmeier, F., Hoffmann, F., Johnson, J. S., Yamaguchi, T., Carslaw, K. S., and Feingold, G.: An emulator
713 approach to stratocumulus susceptibility, *Atmos. Chem. Phys.*, 19, 10191-10203,
714 <https://doi.org/10.5194/acp-19-10191-2019>, 2019.

715 Gleckler, P. J., Doutriaux, C., Durack, P. J., Taylor, K. E., Zhang, Y., Williams, D. N., Mason, E., and
716 Servonnat, J.: A more powerful reality test for climate models, *Eos, Trans. Amer. Geophys. Union*, 97,
717 <https://doi.org/10.1029/2016EO051663>, 2016.

718 Golaz, J.-C., Van Roekel, L. P., Zheng, X., Roberts, A. F., Wolfe, J. D., Lin, W., Bradley, A. M., Tang, Q.,
719 Maltrud, M. E., Forsyth, R. M., Zhang, C., Zhou, T., Zhang, K., Zender, C. S., Wu, M., Wang, H., Turner, A.
720 K., Singh, B., Richter, J. H., Qin, Y., Petersen, M. R., Mametjanov, A., Ma, P.-L., Larson, V. E., Krishna, J.,
721 Keen, N. D., Jeffery, N., Hunke, E. C., Hannah, W. M., Guba, O., Griffin, B. M., Feng, Y., Engwirda, D., Di
722 Vittorio, A. V., Dang, C., Conlon, L. M., Chen, C.-C.-J., Brunke, M. A., Bisht, G., Benedict, J. J., Asay-Davis,
723 X. S., Zhang, Y., Zhang, M., Zeng, X., Xie, S., Wolfram, P. J., Vo, T., Veneziani, M., Tesfa, T. K., Sreepathi, S.,
724 Salinger, A. G., Jack Reeves Eyre, J. E., Prather, M. J., Mahajan, S., Li, Q., Jones, P. W., Jacob, R. L.,
725 Huebler, G. W., Huang, X., Hillman, B. R., Harrop, B. E., Foucar, J. G., Fang, Y., Comeau, D. S., Caldwell, P.
726 M., Bartoletti, T., Balaguru, K., Taylor, M. A., McCoy, R. B., Leung, L. R., and Bader, D. C.: The DOE E3SM
727 Model Version 2: Overview of the physical model and initial model evaluation, *Journal of Advances in*
728 *Modeling Earth Systems*, n/a, e2022MS003156, <https://doi.org/10.1029/2022MS003156>, 2022.

729 Golaz, J.-C., Caldwell, P. M., Van Roekel, L. P., Petersen, M. R., Tang, Q., Wolfe, J. D., Abeshu, G.,
730 Anantharaj, V., Asay-Davis, X. S., Bader, D. C., Baldwin, S. A., Bisht, G., Bogenschutz, P. A., Branstetter,
731 M., Brunke, M. A., Brus, S. R., Burrows, S. M., Cameron-Smith, P. J., Donahue, A. S., Deakin, M., Easter, R.
732 C., Evans, K. J., Feng, Y., Flanner, M., Foucar, J. G., Fyke, J. G., Griffin, B. M., Hannay, C., Harrop, B. E.,
733 Hoffman, M. J., Hunke, E. C., Jacob, R. L., Jacobsen, D. W., Jeffery, N., Jones, P. W., Keen, N. D., Klein, S.
734 A., Larson, V. E., Leung, L. R., Li, H.-Y., Lin, W., Lipscomb, W. H., Ma, P.-L., Mahajan, S., Maltrud, M. E.,
735 Mametjanov, A., McClean, J. L., McCoy, R. B., Neale, R. B., Price, S. F., Qian, Y., Rasch, P. J., Reeves Eyre,
736 J. E. J., Riley, W. J., Ringler, T. D., Roberts, A. F., Roesler, E. L., Salinger, A. G., Shaheen, Z., Shi, X., Singh,
737 B., Tang, J., Taylor, M. A., Thornton, P. E., Turner, A. K., Veneziani, M., Wan, H., Wang, H., Wang, S.,
738 Williams, D. N., Wolfram, P. J., Worley, P. H., Xie, S., Yang, Y., Yoon, J.-H., Zelinka, M. D., Zender, C. S.,
739 Zeng, X., Zhang, C., Zhang, K., Zhang, Y., Zheng, X., Zhou, T., and Zhu, Q.: The DOE E3SM Coupled Model
740 Version 1: Overview and Evaluation at Standard Resolution, *J. Adv. Model. Earth Syst.*, 11, 2089-2129,
741 <https://doi.org/10.1029/2018ms001603>, 2019.

742 Grosvenor, D. P., Sourdeval, O., Zuidema, P., Ackerman, A., Alexandrov, M. D., Bennartz, R., Boers, R.,
743 Cairns, B., Chiu, J. C., Christensen, M., Deneke, H., Diamond, M., Feingold, G., Fridlind, A., Hünerbein, A.,
744 Knist, C., Kollias, P., Marshak, A., McCoy, D., Merk, D., Painemal, D., Rausch, J., Rosenfeld, D.,
745 Russchenberg, H., Seifert, P., Sinclair, K., Stier, P., van Diedenhoven, B., Wendisch, M., Werner, F., Wood,
746 R., Zhang, Z., and Quaas, J.: Remote Sensing of Droplet Number Concentration in Warm Clouds: A
747 Review of the Current State of Knowledge and Perspectives, *Reviews of Geophysics*, 56, 409-453,
748 <https://doi.org/10.1029/2017RG000593>, 2018.

749 Gryspeerd, E., Goren, T., Sourdeval, O., Quaas, J., Mülmenstädt, J., Dipu, S., Unglaub, C., Gettelman, A.,
750 and Christensen, M.: Constraining the aerosol influence on cloud liquid water path, *Atmos. Chem. Phys.*,
751 19, 5331-5347, <https://doi.org/10.5194/acp-19-5331-2019>, 2019.

752 Humphries, R.: MARCUS ARM CN and CCN data reprocessed to remove ship exhaust influence (v2)
753 [dataset], <https://doi.org/10.25919/ezp0-em87>, 2020. Accessed 8 March 2022.

754 Humphries, R. S., McRobert, I. M., Ponsonby, W. A., Ward, J. P., Keywood, M. D., Loh, Z. M., Krummel, P.
755 B., and Harnwell, J.: Identification of platform exhaust on the RV Investigator, *Atmos. Meas. Tech.*, 12,
756 3019-3038, <https://doi.org/10.5194/amt-12-3019-2019>, 2019.

757 IPCC: Climate Change 2021: The Physical Science Basis. Contribution of Working Group I to the Sixth
758 Assessment Report of the Intergovernmental Panel on Climate Change, Cambridge University Press,
759 Cambridge, United Kingdom and New York, NY, USA, 2391 pp.,
760 <https://doi.org/10.1017/9781009157896>, 2021.

761 Jiang, X., Lau, N.-C., and Klein, S. A.: Role of eastward propagating convection systems in the diurnal
762 cycle and seasonal mean of summertime rainfall over the U.S. Great Plains, *Geophys. Res. Lett.*, 33,
763 <https://doi.org/10.1029/2006gl027022>, 2006.

764 Lewis, E. R. and Teixeira, J.: Dispelling clouds of uncertainty, *Eos, Trans. Amer. Geophys. Union*, 96,
765 <https://doi.org/10.1029/2015eo031303>, 2015.

766 Lim, K.-S. S., Riihimaki, L., Comstock, J. M., Schmid, B., Sivaraman, C., Shi, Y., and McFarquhar, G. M.:
767 Evaluation of long-term surface-retrieved cloud droplet number concentration with in situ aircraft
768 observations, *Journal of Geophysical Research: Atmospheres*, 121, 2318-2331,
769 <https://doi.org/10.1002/2015JD024082>, 2016.

770 Ma, P. L., Harrop, B. E., Larson, V. E., Neale, R. B., Gettelman, A., Morrison, H., Wang, H., Zhang, K., Klein,
771 S. A., Zelinka, M. D., Zhang, Y., Qian, Y., Yoon, J. H., Jones, C. R., Huang, M., Tai, S. L., Singh, B.,
772 Bogenschütz, P. A., Zheng, X., Lin, W., Quaas, J., Chepfer, H., Brunke, M. A., Zeng, X., Mülmenstädt, J.,
773 Hagos, S., Zhang, Z., Song, H., Liu, X., Pritchard, M. S., Wan, H., Wang, J., Tang, Q., Caldwell, P. M., Fan, J.,
774 Berg, L. K., Fast, J. D., Taylor, M. A., Golaz, J. C., Xie, S., Rasch, P. J., and Leung, L. R.: Better calibration of
775 cloud parameterizations and subgrid effects increases the fidelity of the E3SM Atmosphere Model
776 version 1, *Geosci. Model Dev.*, 15, 2881-2916, <https://doi.org/10.5194/gmd-15-2881-2022>, 2022.

777 Maloney, E. D., Gettelman, A., Ming, Y., Neelin, J. D., Barrie, D., Mariotti, A., Chen, C. C., Coleman, D. R.
778 B., Kuo, Y.-H., Singh, B., Annamalai, H., Berg, A., Booth, J. F., Camargo, S. J., Dai, A., Gonzalez, A., Hafner,
779 J., Jiang, X., Jing, X., Kim, D., Kumar, A., Moon, Y., Naud, C. M., Sobel, A. H., Suzuki, K., Wang, F., Wang, J.,
780 Wing, A. A., Xu, X., and Zhao, M.: Process-Oriented Evaluation of Climate and Weather Forecasting
781 Models, *Bull. Amer. Meteor. Soc.*, 100, 1665-1686, <https://doi.org/10.1175/bams-d-18-0042.1>, 2019.

782 McFarquhar, G. M., Bretherton, C. S., Marchand, R., Protat, A., DeMott, P. J., Alexander, S. P., Roberts, G.
783 C., Twohy, C. H., Toohey, D., Siems, S., Huang, Y., Wood, R., Rauber, R. M., Lasher-Trapp, S., Jensen, J.,
784 Stith, J. L., Mace, J., Um, J., Järvinen, E., Schnaiter, M., Gettelman, A., Sanchez, K. J., McCluskey, C. S.,
785 Russell, L. M., McCoy, I. L., Atlas, R. L., Bardeen, C. G., Moore, K. A., Hill, T. C. J., Humphries, R. S.,
786 Keywood, M. D., Ristovski, Z., Cravigan, L., Schofield, R., Fairall, C., Mallet, M. D., Kreidenweis, S. M.,
787 Rainwater, B., D'Alessandro, J., Wang, Y., Wu, W., Saliba, G., Levin, E. J. T., Ding, S., Lang, F., Truong, S. C.
788 H., Wolff, C., Haggerty, J., Harvey, M. J., Klekociuk, A. R., and McDonald, A.: Observations of Clouds,
789 Aerosols, Precipitation, and Surface Radiation over the Southern Ocean: An Overview of CAPRICORN,
790 MARCUS, MICRE, and SOCRATES, *Bull. Amer. Meteor. Soc.*, 102, E894-E928,
791 <https://doi.org/10.1175/bams-d-20-0132.1>, 2021.

792 Min, Q. and Harrison, L. C.: Cloud properties derived from surface MFRSR measurements and
793 comparison with GOES results at the ARM SGP Site, *Geophysical Research Letters*, 23, 1641-1644,
794 <https://doi.org/10.1029/96GL01488>, 1996.

795 Minnis, P., Nguyen, L., Palikonda, R., Heck, P. W., Spangenberg, D. A., Doelling, D. R., Ayers, J. K., Smith,
796 J. W. L., Khaiyer, M. M., Trepte, Q. Z., Avey, L. A., Chang, F.-L., Yost, C. R., Chee, T. L., and Szedung, S.-M.:
797 Near-real time cloud retrievals from operational and research meteorological satellites, *Proc. SPIE*
798 *Europe Remote Sens.*, Cardiff, Wales, UK,, 15-18 September, 710703,
799 <https://doi.org/10.1117/12.800344>, 2008.

800 Minnis, P., Sun-Mack, S., Young, D. F., Heck, P. W., Garber, D. P., Chen, Y., Spangenberg, D. A., Arduini, R.
801 F., Trepte, Q. Z., Smith, W. L., Ayers, J. K., Gibson, S. C., Miller, W. F., Hong, G., Chakrapani, V., Takano, Y.,
802 Liou, K. N., Xie, Y., and Yang, P.: CERES Edition-2 Cloud Property Retrievals Using TRMM VIRS and Terra
803 and Aqua MODIS Data—Part I: Algorithms, *IEEE Transactions on Geoscience and Remote Sensing*, 49,
804 4374-4400, <https://doi.org/10.1109/TGRS.2011.2144601>, 2011.

805 Myhre, G., Samset, B. H., Schulz, M., Balkanski, Y., Bauer, S., Bernsten, T. K., Bian, H., Bellouin, N., Chin,
806 M., Diehl, T., Easter, R. C., Feichter, J., Ghan, S. J., Hauglustaine, D., Iversen, T., Kinne, S., Kirkevåg, A.,
807 Lamarque, J. F., Lin, G., Liu, X., Lund, M. T., Luo, G., Ma, X., van Noije, T., Penner, J. E., Rasch, P. J., Ruiz,
808 A., Seland, Ø., Skeie, R. B., Stier, P., Takemura, T., Tsigaridis, K., Wang, P., Wang, Z., Xu, L., Yu, H., Yu, F.,
809 Yoon, J. H., Zhang, K., Zhang, H., and Zhou, C.: Radiative forcing of the direct aerosol effect from
810 AeroCom Phase II simulations, *Atmos. Chem. Phys.*, 13, 1853-1877, [https://doi.org/10.5194/acp-13-](https://doi.org/10.5194/acp-13-1853-2013)
811 [1853-2013](https://doi.org/10.5194/acp-13-1853-2013), 2013.

812 NETCDF: Introduction and Overview: <https://www.unidata.ucar.edu/software/netcdf/docs/index.html>,
813 last access: 12 November 2022. 2022.

814 Quaas, J., Boucher, O., Bellouin, N., and Kinne, S.: Satellite-based estimate of the direct and indirect
815 aerosol climate forcing, *Journal of Geophysical Research: Atmospheres*, 113,
816 <https://doi.org/10.1029/2007JD008962>, 2008.

817 Rasch, P. J., Xie, S., Ma, P.-L., Lin, W., Wang, H., Tang, Q., Burrows, S. M., Caldwell, P., Zhang, K., Easter,
818 R. C., Cameron-Smith, P., Singh, B., Wan, H., Golaz, J.-C., Harrop, B. E., Roesler, E., Bacmeister, J., Larson,
819 V. E., Evans, K. J., Qian, Y., Taylor, M., Leung, L. R., Zhang, Y., Brent, L., Branstetter, M., Hannay, C.,
820 Mahajan, S., Mامتjanov, A., Neale, R., Richter, J. H., Yoon, J.-H., Zender, C. S., Bader, D., Flanner, M.,
821 Foucar, J. G., Jacob, R., Keen, N., Klein, S. A., Liu, X., Salinger, A. G., Shrivastava, M., and Yang, Y.: An
822 Overview of the Atmospheric Component of the Energy Exascale Earth System Model, *J. Adv. Model.*
823 *Earth Syst.*, 11, 2377-2411, <https://doi.org/10.1029/2019ms001629>, 2019.

824 Reddington, C. L., Carslaw, K. S., Stier, P., Schutgens, N., Coe, H., Liu, D., Allan, J., Browse, J., Pringle, K. J.,
825 Lee, L. A., Yoshioka, M., Johnson, J. S., Regayre, L. A., Spracklen, D. V., Mann, G. W., Clarke, A., Hermann,
826 M., Henning, S., Wex, H., Kristensen, T. B., Leaitch, W. R., Pöschl, U., Rose, D., Andreae, M. O., Schmale,
827 J., Kondo, Y., Oshima, N., Schwarz, J. P., Nenes, A., Anderson, B., Roberts, G. C., Snider, J. R., Leck, C.,
828 Quinn, P. K., Chi, X., Ding, A., Jimenez, J. L., and Zhang, Q.: The Global Aerosol Synthesis and Science
829 Project (GASSP): Measurements and Modeling to Reduce Uncertainty, *Bull. Amer. Meteor. Soc.*, 98,
830 1857-1877, <https://doi.org/10.1175/bams-d-15-00317.1>, 2017.

831 Riihimaki, L., McFarlane, S., and Sivaraman, C.: Droplet Number Concentration Value-Added Product,
832 ARM Research Facility, Report number: DOE/SC-ARM-TR-140, 2021.

833 Schulz, M., Textor, C., Kinne, S., Balkanski, Y., Bauer, S., Bernsten, T., Berglen, T., Boucher, O., Dentener,
834 F., Guibert, S., Isaksen, I. S. A., Iversen, T., Koch, D., Kirkevåg, A., Liu, X., Montanaro, V., Myhre, G.,
835 Penner, J. E., Pitari, G., Reddy, S., Seland, Ø., Stier, P., and Takemura, T.: Radiative forcing by aerosols as
836 derived from the AeroCom present-day and pre-industrial simulations, *Atmos. Chem. Phys.*, 6, 5225-
837 5246, <https://doi.org/10.5194/acp-6-5225-2006>, 2006.

838 Song, X., Zhang, G. J., and Li, J. L. F.: Evaluation of Microphysics Parameterization for Convective Clouds
839 in the NCAR Community Atmosphere Model CAM5, *J. Climate*, 25, 8568-8590,
840 <https://doi.org/10.1175/JCLI-D-11-00563.1>, 2012.

841 Sun, J., Zhang, K., Wan, H., Ma, P.-L., Tang, Q., and Zhang, S.: Impact of Nudging Strategy on the Climate
842 Representativeness and Hindcast Skill of Constrained EAMv1 Simulations, *J. Adv. Model. Earth Syst.*, 11,
843 3911-3933, <https://doi.org/10.1029/2019MS001831>, 2019.

844 Tang, Q., Klein, S. A., Xie, S., Lin, W., Golaz, J. C., Roesler, E. L., Taylor, M. A., Rasch, P. J., Bader, D. C.,
845 Berg, L. K., Caldwell, P., Giangrande, S. E., Neale, R. B., Qian, Y., Riihimaki, L. D., Zender, C. S., Zhang, Y.,
846 and Zheng, X.: Regionally refined test bed in E3SM atmosphere model version 1 (EAMv1) and
847 applications for high-resolution modeling, *Geosci. Model Dev.*, 12, 2679-2706,
848 <https://doi.org/10.5194/gmd-12-2679-2019>, 2019.

849 Tang, S., Zhang, M., and Xie, S.: An ensemble constrained variational analysis of atmospheric forcing
850 data and its application to evaluate clouds in CAM5, *J. Geophys. Res. Atmos.*, 121, 33-48,
851 <https://doi.org/10.1002/2015JD024167>, 2016.

852 Tang, S., Gleckler, P., Xie, S., Lee, J., Ahn, M.-S., Covey, C., and Zhang, C.: Evaluating the Diurnal and
853 Semidiurnal Cycle of Precipitation in CMIP6 Models Using Satellite- and Ground-Based Observations, *J.*
854 *Climate*, 34, 3189-3210, <https://doi.org/10.1175/jcli-d-20-0639.1>, 2021.

855 Tang, S., Fast, J. D., Zhang, K., Hardin, J. C., Varble, A. C., Shilling, J. E., Mei, F., Zawadowicz, M. A., and
856 Ma, P. L.: Earth System Model Aerosol-Cloud Diagnostics (ESMAC Diags) package, version 1: assessing
857 E3SM aerosol predictions using aircraft, ship, and surface measurements, *Geosci. Model Dev.*, 15, 4055-
858 4076, <https://doi.org/10.5194/gmd-15-4055-2022>, 2022a.

859 Tang, S., Xie, S., Guo, Z., Hong, S.-Y., Khouider, B., Klocke, D., Köhler, M., Koo, M.-S., Krishna, P. M.,
860 Larson, V. E., Park, S., Vaillancourt, P. A., Wang, Y.-C., Yang, J., Daleu, C. L., Homeyer, C. R., Jones, T. R.,
861 Malap, N., Negggers, R., Prabhakaran, T., Ramirez, E., Schumacher, C., Tao, C., Bechtold, P., Ma, H.-Y.,
862 Neelin, J. D., and Zeng, X.: Long-term single-column model intercomparison of diurnal cycle of
863 precipitation over midlatitude and tropical land, *Quarterly Journal of the Royal Meteorological Society*,
864 148, 641-669, <https://doi.org/10.1002/qj.4222>, 2022b.

865 Turner, D. D., Lo, C., Min, Q., Zhang, D., and Gaustad, K.: Cloud Optical Properties from the Multifilter
866 Shadowband Radiometer (MFRSRCLDOD): An ARM Value-Added Product, ARM Research Facility, Report
867 number: DOE/SC-ARM-TR-047, 2021.

868 Varble, A. C., Ma, P. L., christensen, M. W., Mülmenstädt, J., Tang, S., and Fast, J. D.: Evaluation of Liquid
869 Cloud Albedo Susceptibility in E3SM Using Coupled Eastern North Atlantic Surface and Satellite
870 Retrievals, *Atmos. Chem. Phys.*, submitted, 2023.

871 Wang, J., Wood, R., Jensen, M. P., Chiu, J. C., Liu, Y., Lamer, K., Desai, N., Giangrande, S. E., Knopf, D. A.,
872 Kollias, P., Laskin, A., Liu, X., Lu, C., Mechem, D., Mei, F., Starzec, M., Tomlinson, J., Wang, Y., Yum, S. S.,
873 Zheng, G., Aiken, A. C., Azevedo, E. B., Blanchard, Y., China, S., Dong, X., Gallo, F., Gao, S., Ghate, V. P.,
874 Glienke, S., Goldberger, L., Hardin, J. C., Kuang, C., Luke, E. P., Matthews, A. A., Miller, M. A., Moffet, R.,
875 Pekour, M., Schmid, B., Sedlacek, A. J., Shaw, R. A., Shilling, J. E., Sullivan, A., Suski, K., Veghte, D. P.,
876 Weber, R., Wyant, M., Yeom, J., Zawadowicz, M., and Zhang, Z.: Aerosol and Cloud Experiments in the
877 Eastern North Atlantic (ACE-ENA), *Bull. Amer. Meteor. Soc.*, 1-51, [https://doi.org/10.1175/bams-d-19-](https://doi.org/10.1175/bams-d-19-0220.1)
878 [0220.1](https://doi.org/10.1175/bams-d-19-0220.1), 2021.

879 Watson-Parris, D., Schutgens, N., Reddington, C., Pringle, K. J., Liu, D., Allan, J. D., Coe, H., Carslaw, K. S.,
880 and Stier, P.: In situ constraints on the vertical distribution of global aerosol, *Atmos. Chem. Phys.*, 19,
881 11765-11790, <https://doi.org/10.5194/acp-19-11765-2019>, 2019.

882 Wu, P., Dong, X., Xi, B., Tian, J., and Ward, D. M.: Profiles of MBL Cloud and Drizzle Microphysical
883 Properties Retrieved From Ground-Based Observations and Validated by Aircraft In Situ Measurements
884 Over the Azores, *Journal of Geophysical Research: Atmospheres*, 125, e2019JD032205,
885 <https://doi.org/10.1029/2019JD032205>, 2020.

886 Xie, S., Lin, W., Rasch, P. J., Ma, P.-L., Neale, R., Larson, V. E., Qian, Y., Bogenschütz, P. A., Caldwell, P.,
887 Cameron-Smith, P., Golaz, J.-C., Mahajan, S., Singh, B., Tang, Q., Wang, H., Yoon, J.-H., Zhang, K., and
888 Zhang, Y.: Understanding Cloud and Convective Characteristics in Version 1 of the E3SM Atmosphere
889 Model, *J. Adv. Model. Earth Syst.*, 10, 2618-2644, <https://doi.org/10.1029/2018MS001350>, 2018.

890 Xu, K.-M. and Cheng, A.: Evaluating Low-Cloud Simulation from an Upgraded Multiscale Modeling
891 Framework Model. Part II: Seasonal Variations over the Eastern Pacific, *J. Climate*, 26, 5741-5760,
892 <https://doi.org/10.1175/JCLI-D-12-00276.1>, 2013a.

893 Xu, K.-M. and Cheng, A.: Evaluating Low-Cloud Simulation from an Upgraded Multiscale Modeling
894 Framework Model. Part I: Sensitivity to Spatial Resolution and Climatology, *J. Climate*, 26, 5717-5740,
895 <https://doi.org/10.1175/JCLI-D-12-00200.1>, 2013b.

896 Zhang, C., Xie, S., Tao, C., Tang, S., Emmenegger, T., Neelin, J. D., Schiro, K. A., Lin, W., and Shaheen, Z.:
897 The ARM Data-Oriented Metrics and Diagnostics Package for Climate Models: A New Tool for Evaluating
898 Climate Models with Field Data, *Bull. Amer. Meteor. Soc.*, 101, E1619-E1627,
899 <https://doi.org/10.1175/bams-d-19-0282.1>, 2020.

900 Zhang, S., Zhang, K., Wan, H., and Sun, J.: Further improvement and evaluation of nudging in the E3SM
901 Atmosphere Model version 1 (EAMv1): simulations of the mean climate, weather events, and
902 anthropogenic aerosol effects, *Geosci. Model Dev.*, 15, 6787-6816, [https://doi.org/10.5194/gmd-15-](https://doi.org/10.5194/gmd-15-6787-2022)
903 [6787-2022](https://doi.org/10.5194/gmd-15-6787-2022), 2022.

904 Zhang, Y., Xie, S., Lin, W., Klein, S. A., Zelinka, M., Ma, P.-L., Rasch, P. J., Qian, Y., Tang, Q., and Ma, H.-Y.:
905 Evaluation of Clouds in Version 1 of the E3SM Atmosphere Model With Satellite Simulators, *Journal of*
906 *Advances in Modeling Earth Systems*, 11, 1253-1268, <https://doi.org/10.1029/2018MS001562>, 2019.

907 Zhou, X., Kollias, P., and Lewis, E. R.: Clouds, Precipitation, and Marine Boundary Layer Structure during
908 the MAGIC Field Campaign, *J. Climate*, 28, 2420-2442, <https://doi.org/10.1175/jcli-d-14-00320.1>, 2015.

909